The WiggleZ Dark Energy Survey: star formation in UV-luminous galaxies from their luminosity functions

Russell J. Jurek,[1,2]★ Michael J. Drinkwater,[2] Kevin Pimbblet,[3] Karl Glazebrook,[4] Chris Blake,[4] Sarah Brough,[5] Matthew Colless,[5] Carlos Contreras,[4] Warrick Couch,[4] Scott Croom,[6] Darren Croton,[4] Tamara M. Davis,[2] Karl Forster,[7] David Gilbank,[8] Mike Gladders,[9] Ben Jelliffe,[6] I-hui Li,[1] Barry Madore,[10] D. Christopher Martin,[7] Gregory B. Poole,[4] Michael Pracy,[6] Rob Sharp,[11] Emily Wisnioski,[4,12] David Woods,[13] Ted K. Wyder[7] and H. K. C. Yee[14]

[1]*CSIRO Astronomy & Space Science, Australia Telescope National Facility, Sydney, NSW 2112, Australia*
[2]*School of Mathematics and Physics, University of Queensland, Brisbane, QLD 4072, Australia*
[3]*School of Physics, Monash University, Clayton, VIC 3800, Australia*
[4]*Centre for Astrophysics & Supercomputing, Swinburne University of Technology, PO Box 218, Hawthorn, VIC 3122, Australia*
[5]*Australian Astronomical Observatory, PO Box 915, North Ryde, NSW 1670, Australia*
[6]*Sydney Institute for Astronomy, School of Physics, University of Sydney, NSW 2006, Australia*
[7]*California Institute of Technology, MC 278-17, 1200 East California Boulevard, Pasadena, CA 91125, USA*
[8]*South African Astronomical Observatory, PO Box 9, Observatory 7935, South Africa*
[9]*Department of Astronomy and Astrophysics, University of Chicago, 5640 South Ellis Avenue, Chicago, IL 60637, USA*
[10]*Observatories of the Carnegie Institute of Washington, 813 Santa Barbara St, Pasadena, CA 91101, USA*
[11]*Research School of Astronomy & Astrophysics, Australian National University, Weston Creek, ACT 2611, Australia*
[12]*Max-Planck-Institut für extraterrestrische Physik (MPE), Giessenbachstr. 1, D-85748 Garching, Germany*
[13]*Department of Physics & Astronomy, University of British Columbia, 6224 Agricultural Road, Vancouver, BC V6T 1Z1, Canada*
[14]*Department of Astronomy and Astrophysics, University of Toronto, 50 St George Street, Toronto, ON M5S 3H4, Canada*

ABSTRACT

We present the ultraviolet (UV) luminosity function of galaxies from the *GALEX* Medium Imaging Survey with measured spectroscopic redshifts from the first data release of the WiggleZ Dark Energy Survey. Our sample consists of 39 996 NUV < 22.8 emission line galaxies in the redshift range $0.1 < z < 0.9$. This sample selects galaxies with high star formation rates: at $0.6 < z < 0.9$ the median star formation rate is at the upper 95th percentile of optically selected ($r < 22.5$) galaxies and the sample contains about 50 per cent of all NUV < 22.8, $0.6 < z < 0.9$ starburst galaxies within the volume sampled. The most luminous galaxies in our sample ($-21.0 > M_{\mathrm{NUV}} > -22.5$) evolve very rapidly with a number density declining as $(1 + z)^{5\pm1}$ from redshift $z = 0.9$ to 0.6. These starburst galaxies ($M_{\mathrm{NUV}} < -21$ is approximately a star formation rate of $30\,\mathrm{M_\odot\,yr^{-1}}$) contribute about 1 per cent of cosmic star formation over the redshift range $z = 0.6$–0.9. The star formation rate density of these very luminous galaxies evolves rapidly, as $(1 + z)^{4\pm1}$. Such a rapid evolution implies that the majority of star formation in these large galaxies must have occurred before $z = 0.9$. We measure the UV luminosity function in $\Delta z = 0.05$ redshift intervals spanning $0.1 < z < 0.9$, and provide analytic fits to the results. Our measurements of the luminosity function over this redshift range probe further into the bright end (1–2 mag further) than previous measurements, e.g. Arnouts et al., Budavári et al. and Treyer et al., due to our much larger sample size and sampled volume. At all redshifts $z > 0.55$ we find that the bright end of the luminosity function is not well described by a pure Schechter function due to an excess of very luminous

★ E-mail: Russell.Jurek@gmail.com

($M_{\mathrm{NUV}} < -22$) galaxies. These luminosity functions can be used to create a radial selection function for the WiggleZ survey or test models of galaxy formation and evolution. Here we test the AGN feedback model in Scannapieco, Silk & Bouwens, and find that this AGN feedback model requires AGN feedback efficiency to vary with one or more of the following: stellar mass, star formation rate and redshift.

Key words: galaxies: luminosity function, mass function – galaxies: starburst – ultraviolet: galaxies.

1 INTRODUCTION

Many recent studies have measured a rapid rise in the global star formation rate (SFR) moving from the present epoch back to redshifts of $z \sim 1$ (as reviewed by Hopkins 2004). These studies have generally used different measurements of SFR for galaxies at different redshifts, driven by what could be measured in the optical region of the *observed wavelength* spectra. The *rest-wavelength* ultraviolet (UV) luminosity of galaxies is an important indicator of SFR (e.g. Kennicutt 1998) and is the most common method at high redshifts (Hopkins 2004), but until recently very few UV measurements had been made of low-redshift galaxy populations.

The *Galaxy Evolution Explorer* (*GALEX*; see Martin et al. 2005) satellite with its far-UV (FUV; 1350–1750 Å) and near-UV (NUV; 1750–2750 Å) cameras has permitted extensive UV measurements of star formation at low redshifts. This work started with several measurements of the low-redshift ($z < 0.25$) UV luminosity function (LF; Budavári et al. 2005; Treyer et al. 2005; Wyder et al. 2005). Wyder et al. (2005) measured a SFR density about half that of earlier Hα results (Gallego et al. 1995) when using an extinction correction of $A_{\mathrm{FUV}} \approx 1$ but noted that the results were consistent considering the uncertainties, especially in the assumed extinction.

The *GALEX* studies were extended to higher redshifts ($0.2 < z < 1.2$) by using a sample of 1309 galaxies from a spectroscopic survey overlapping a deep *GALEX* field (Arnouts et al. 2005; Schiminovich et al. 2005). The sample exhibited strong evolution in the FUV luminosity density of the form $(1 + z)^{2.5}$ up to $z \approx 1$, with the most UV-luminous galaxies evolving even faster [$\sim (1 + z)^5$]. The most luminous galaxies ($M < -19.3$) were found to contribute as much as 25 per cent of the total luminosity density by a redshift of $z \sim 1$ (Schiminovich et al. 2005).

The rapid evolution of the contribution of massive galaxies has been investigated in a series of studies of how SFRs evolve with redshift and stellar mass. Noeske et al. (2007a) measured SFRs for some 3000 galaxies with spectroscopic redshifts from the All-wavelength Extended Groth strip International Survey (AEGIS; Davis et al. 2007). They found a relatively tight relation between SFRs and stellar mass (the 'main sequence of star formation'). This sequence keeps a constant slope but moves to lower rates with decreasing redshift. This evolution was modelled in terms of the specific SFRs fading in all galaxies due to gas exhaustion, but with the peak of star formation occurring later (at lower redshift) for smaller galaxies (Noeske et al. 2007b).

Mobasher et al. (2009) obtained similar results from a study of 66 500 galaxies with photometric redshifts. Although they found that the relative contribution of massive galaxies to the total SFR remains constant out to $z \sim 1$, the 'characteristic' SFR (i.e. per galaxy) drops by an order of magnitude from $z = 1$ to 0.3. More importantly, they found that the contribution of massive galaxies to the overall SFR density was very small, indicating that the massive galaxies must have formed the bulk of their stars at earlier epochs,

consistent with the results from the UV-selected samples (Arnouts et al. 2005).

A major consequence of these observations is that if the most massive galaxies formed the vast bulk of their stars at epochs earlier than $z \approx 1$, then they should contribute a negligible fraction of the total SFR density at later times. This is suggested by some of the observations (notably by Arnouts et al. 2005), but for the most massive galaxies the samples are very small, due to the small volumes sampled.

In this paper we use a new, very large volume sample of UV-luminous galaxies to measure the contribution of UV-luminous galaxies to the Universe star formation over the redshift range $0.1 < z < 0.9$, and the contribution of the most massive UV-luminous galaxies over $0.6 < z < 0.9$. Our galaxy sample is taken from early observations of the WiggleZ Dark Energy Survey of UV-selected galaxies using the AAOmega multi-object spectrograph on the 3.9 m Anglo-Australian Telescope (Drinkwater et al. 2010).

The galaxy sample we analyse in this paper is over 40 times larger than that of Arnouts et al. (2005) and so allows us to detect much rarer galaxies. In addition to measuring the contribution of these UV-luminous galaxies to the overall SFR of the Universe, we also determine the LF of these galaxies. These LFs can be used for a variety of purposes, such as testing semi-analytic models of galaxy formation and evolution, or generating a radial selection function for the WiggleZ survey.

In Section 2, we describe the sample of galaxies used, as well as our method of estimating SFRs. In Section 3, we discuss the completeness of the galaxy sample and show what subsample of all galaxies is selected. We present the LFs of the WiggleZ galaxies in Section 4. In Section 5, we analyse the LFs and discuss the implications of the results, notably the evolution of star formation in the most massive galaxies in our sample and their contribution to the overall SFR. We summarize the main results in Section 6.

A standard cosmology of $\Omega_{\mathrm{m}} = 0.3$, $\Omega_{\Lambda} = 0.7$ and $h = 0.72$ is adopted throughout this paper.

2 DATA SET

The WiggleZ survey is described in detail by Drinkwater et al. (2010). Here we present a brief review of the properties of the WiggleZ survey relevant to this work. In this paper, we analyse the WiggleZ data set observed prior to 2009 April that used data from the Sloan Digital Sky Survey (SDSS) Data Release 5 (Adelman-McCarthy et al. 2006) for the optical photometry. The corresponding regions on the sky are listed in Table 1, and the criteria used to select targets for spectroscopic follow-up from the combination of UV and optical photometry are presented in Table 2. The spectroscopic observations were prioritized to observe fainter targets first, according to the optical *r*-band magnitudes as listed in Table 2.

The three regions contained 340 *GALEX* tiles and 73 793 WiggleZ targets. Spectroscopic observations obtained a reliable redshift for 45 869 of these targets. For details of the spectroscopic observations,

Table 1. The survey boundaries of the three WiggleZ regions analysed.

Rectangle ID	RA range (deg, J2000)	Dec. range (deg, J2000)
09 h	$133.7 \leq RA \leq 148.8$	$-1 \leq Dec. \leq 8.1$
11 h	$153 \leq RA \leq 172$	$-1 \leq Dec. \leq 8$
15 h	$210 \leq RA \leq 230$	$-3 \leq Dec. \leq 7$

Table 2. The target selection criterion and prioritization scheme used by the WiggleZ survey, to select $z > 0.5$ emission line galaxies for spectroscopic follow-up from the combination of *GALEX* UV and SDSS optical photometry.

Property	Criterion
NUV	$NUV < 22.8$
r	$20 \leq r \leq 22.5$
$FUV - NUV$	$FUV - NUV > 1$ or FUV dropout
$NUV - r$	$-0.5 \leq NUV - r \leq 2$
NUV flux S/N	$S/N \geq 3$
LRR[1] criterion	$(r - i > g - r - 0.1)$ or $(r - i > 0.4)$ or $(g > 22.5)$ or $(i > 21.5)$
Quasar?	Not flagged as a quasar
Priority 8	$22 < r \leq 22.5$
Priority 7	$21.5 < r \leq 22$
Priority 6	$21 < r \leq 21.5$
Priority 5	$20.5 < r \leq 21$
Priority 4	$20 \leq r \leq 20.5$

Note: (1): the low-redshift rejection (LRR) criterion uses optical photometry to reduce the number of low-redshift targets.

Figure 1. WiggleZ galaxy luminosities as a function of redshift. The survey selection limits in apparent NUV and r magnitude are shown as dashed lines. The solid green lines show M^* values from fits to the LFs at each redshift (with faint-end slopes fixed at $\alpha = -1$; see Section 4.1).

Figure 2. The SFRs for the galaxies in our sample as a function of redshift. The inset is an enlargement of the bottom-right corner showing that the sample contains significant numbers of starburst ($SFR > 30\,M_\odot\,yr^{-1}$) galaxies at $z > 0.5$. In both the red line marks the starburst galaxy criterion of Cowie et al. (1996) ($SFR > 30\,M_\odot\,yr^{-1}$).

redshift measurements and the reliability of these redshifts, we refer the reader to Drinkwater et al. (2010). In summary, we inspected all the WiggleZ spectra manually and gave the final redshift a quality number (Q) from 1 to 5. A reliable redshift corresponds to $Q \geq 3$. The Q values of 3, 4 and 5 correspond to 83, 99 and 99.9 per cent of the redshifts being correctly measured. Any galaxies with broad emission lines were flagged as quasars at the inspection stage. These objects were removed from the sample analysed in this paper as our aim is to measure just the starburst galaxy population.

We restrict the redshift range of our sample to $0.1 < z < 0.9$ for two reasons. First, Blake et al. (2009) found that most of the redshift errors result in a galaxy being incorrectly assigned a $z > 0.9$ redshift. Secondly, this removes remaining stars and quasars in our sample that were not identified and flagged during redshifting. Using the identified quasars as a test case, we find that the $z < 0.9$ redshift cut removes 85 per cent of the identified quasars. It is important to note that this is indicative only. An arbitrary fraction of $z < 0.9$ quasars may remain in our sample. The $z > 0.1$ limit removes 82 per cent of all identified stars (mainly M-dwarfs) from our sample. Applying these redshift cuts, we reduce the size of our sample slightly to 39 996 targets but remove most stars, quasars and incorrect redshifts.

We calculated luminosities of the galaxies in each band using *k*-corrections calculated with the *kcorrect v4.1.4* library (Blanton & Roweis 2007). We based the FUV luminosities on the NUV magnitudes because many of the galaxies in our sample were not detected in the FUV. For a complete description see Appendix A1. We show the distribution of absolute NUV and *R* magnitudes as a function of redshift for the sample in Fig. 1. The figure demonstrates
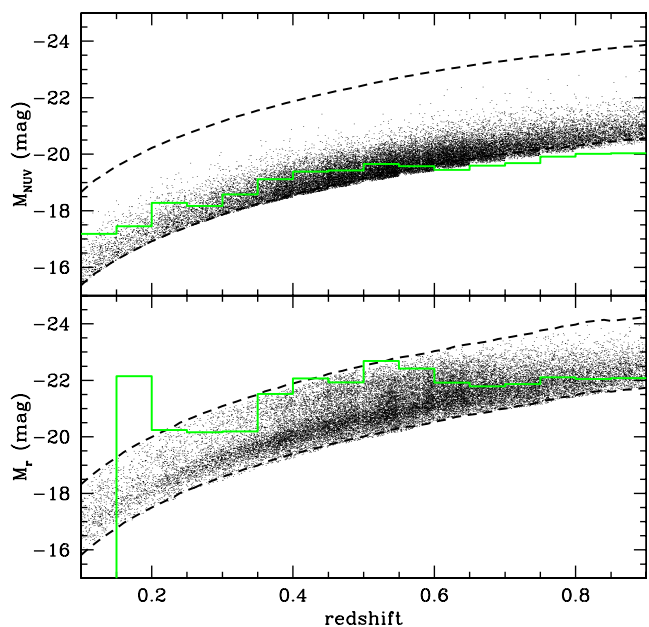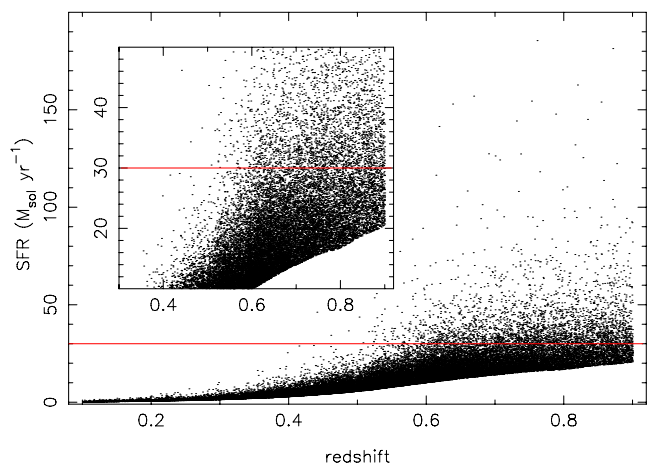
the relatively narrow range of luminosity sampled by the survey at any given redshift.

We estimated SFRs for the galaxies from their UV (1500–2500 Å) specific luminosities corrected for intrinsic dust extinction using the β–IRX relation (Calzetti, Kinney & Storchi-Bergmann 1994; Meurer, Heckman & Calzetti 1999; Calzetti et al. 2000). We present details of these calculations in Appendix A. The resulting SFRs for the sample are shown in Fig. 2. The figure shows that our sample contains significant numbers of starburst galaxies at redshifts above 0.5 [using the Cowie et al. (1996) definition of a starburst galaxy as one with $SFR > 30\,M_\odot\,yr^{-1}$].

We have calculated the SFRs that would correspond to luminous infrared galaxies (LIRGs) and ultraluminous infrared galaxies

(ULIRGs), and compared them to the SFRs of WiggleZ galaxies. In Sanders & Mirabel (1996), LIRGs and ULIRGS are defined as having infrared luminosities (over 8–1000 μm), exceeding 10^{11} and 10^{12} solar luminosities. Using equation 4 of Kennicutt (1998), we have calculated that LIRGs and ULIRGs undergoing a starburst have SFRs exceeding 17.2 and 172 $M_\odot$ yr^{-1}. Equation 4 of Kennicutt (1998) can be modified to apply to quiescent Sb and later galaxies using the results in Buat & Xu (1996). Sb and later LIRGs and ULIRGs have SFRs exceeding 36 and 360 $M_\odot$ yr^{-1}. Irrespective of galaxy type, the SFRs of WiggleZ starburst galaxies therefore match those of LIRGs but not ULIRGs. However, two of the WiggleZ galaxies in Fig. 2 have SFRs consistent with ULIRGs.

3 COMPARISON OF WIGGLEZ GALAXIES TO OTHER SAMPLES

The NUV flux limit of the WiggleZ survey tends to select starforming galaxies, but the additional low-redshift rejection (LRR) colour limits give a complex selection function. In this section, we compare the WiggleZ galaxy sample to two reference samples defined by simple optical and UV flux limits. We use the optical sample ($R < 22.5$) to compare the WiggleZ galaxies to the entire underlying galaxy population. The UV sample (NUV < 22.8) allows us to determine how well the WiggleZ galaxies trace the starburst galaxy population.

We selected both reference samples from the AEGIS region of the DEEP2 survey (Davis et al. 2003, 2007). In addition to the DEEP2 imaging and spectroscopy, this region has very deep UV [90 separate *GALEX* exposures at the Medium Imaging Survey (MIS) depth] and optical (Canada–France–Hawaii Telescope Legacy Survey, CFHTLS; Martin et al. 2007) imaging. We simulated the WiggleZ sample that would be selected in this region by taking the mean counts after applying our selection criteria to the separate *GALEX* exposures. We provide details of the two reference samples and the weighting scheme that accounts for the DEEP2 spectroscopic completeness in Appendix B.

We find that WiggleZ (in the SDSS regions) selects 1.76 ± 0.05 per cent of $0.1 < z < 0.9$ and 3.34 ± 0.11 per cent of $0.6 < z < 0.9$, $R < 22.5$ optical galaxies. The uncertainty in these fractions is calculated assuming binomial statistics and propagating the uncertainty in the DEEP2 spectroscopic weights. These percentages can be understood by examining the effect of various WiggleZ selection cuts on $R < 12.5$, $21.5 < R < 22.5$ and $R < 22.5$ galaxies, which are presented in Table 3. We find that requiring $R < 22.5$ galaxies to be S/N ≥ 3, NUV < 22.8 *GALEX* MIS detections removes the majority of them at all redshifts. The remaining WiggleZ cuts remove ~ 90 and ~ 50 per cent of the S/N ≥ 3, NUV < 22.8, $R < 22.5$ galaxies over $0.1 < z < 0.9$ and $0.6 < z < 0.9$.

Table 3 also shows that each of the NUV detection, NUV < 22.8 and S/N ≥ 3 requirements removes more $21.5 < R < 22.5$ galaxies than $R < 21.5$ galaxies, at all redshifts. We propose that this is responsible for fig. 8 of Drinkwater et al. (2010). Drinkwater et al. (2010) found that the median R magnitude of WiggleZ galaxies is around 1 mag brighter than the $R < 22.5$ limit of our reference sample.

To characterize which galaxies are selected by WiggleZ from the optical reference sample, we compared the median SFRs of the respective samples as a function of redshift. The median values for both the WiggleZ and reference galaxies are scaled by the DEEP2 spectroscopic completeness weights. We calculated the

Table 3. The fraction of $R < 21.5$, $21.5 < R < 22.5$ and $R < 22.5$ galaxies satisfying various WiggleZ selection cuts. The fraction of these galaxy subsets that are eventually selected by WiggleZ is also shown.

Additional cut/s	$0.1 < z < 0.9$ Per cent remain	Per cent WGZ	$0.6 < z < 0.9$ Per cent remain	Per cent WGZ
R < 22.5 galaxies selected				
None	100	1.76 ± 0.05	100	3.34 ± 0.11
+ NUV detection	39.31 ± 0.11	4.48 ± 0.13	30.39 ± 0.19	11.0 ± 0.4
+ NUV <22.8	17.47 ± 0.09	10.1 ± 0.3	8.46 ± 0.13	39.5 ± 1.3
+ NUV S/N $\geq$3	15.23 ± 0.09	11.6 ± 0.3	6.46 ± 0.12	51.7 ± 1.7
+ WGZ[1]	1.76 ± 0.05	100	3.34 ± 0.11	100
R < 21.5 galaxies selected				
None	100	2.16 ± 0.15	100	8.9 ± 0.5
+ NUV detection	48.6 ± 0.2	4.4 ± 0.3	46.1 ± 0.7	19.4 ± 1.1
+ NUV <22.8	31.8 ± 0.2	6.8 ± 0.5	20.6 ± 0.6	43 ± 2
+ NUV S/N $\geq$3	29.2 ± 0.2	7.4 ± 0.5	17.3 ± 0.6	51 ± 3
+ WGZ[1]	2.16 ± 0.15	100	8.9 ± 0.5	100
$21.5 < R < 22.5$ galaxies selected				
None	100	1.67 ± 0.07	100	2.04 ± 0.11
+ NUV detection	32.72 ± 0.16	5.1 ± 0.2	26.9 ± 0.2	7.6 ± 0.4
+ NUV <22.8	7.6 ± 0.1	22.0 ± 1.0	5.87 ± 0.14	34.7 ± 1.9
+ NUV S/N $\geq$3	5.4 ± 0.1	30.7 ± 1.4	4.06 ± 0.13	50 ± 3
+ WGZ[1]	1.67 ± 0.08	100	2.04 ± 0.11	100

Note (1): WGZ refers to the remaining selection criteria listed in Table 2.

SFRs from the *B* magnitudes for consistency, because not all the DEEP2 galaxies are matched to a *GALEX* source. We used a cross *k*-correction from the *B* band to a 1500–2500 Å top-hat filter, and then applied the Kennicutt relation (Kennicutt 1998). We do not correct for the internal dust extinction, because we do not have the data to apply a consistent correction to all galaxies in the optical sample. The results in Fig. 3 show that the median SFR of WiggleZ galaxies is greater than that of the optical galaxies at all redshifts: the WiggleZ selection criteria identify star-forming galaxies as desired. Fig. 3 does, however, reveal a change in the WiggleZ selection at $z \sim 0.6$. WiggleZ galaxies are among the most highly star-forming galaxies at $z > 0.6$ (the median SFR is at the 95th percentile of the optical sample), but this drops to only around the 75th percentile at $z < 0.6$. This decrease in the median WiggleZ SFR at $z < 0.6$ is a consequence of using the LRR cuts, which we found preferentially removes galaxies from the sample that are bluer in NUV $- r$ for a given $g - r$ colour. This was not considered during design of the LRR cuts and is an unintended side effect.

Finally, we assess how well the WiggleZ galaxies trace the starburst galaxy population (defined as galaxies with SFR > 30 $M_\odot$ yr^{-1}; Cowie et al. 1996). We calculated the SFRs from the NUV magnitudes, but (as above) did not calculate individual dust corrections for each galaxy. We instead used a constant correction of 1 mag of extinction (based on Fig. A2, Appendix A2)
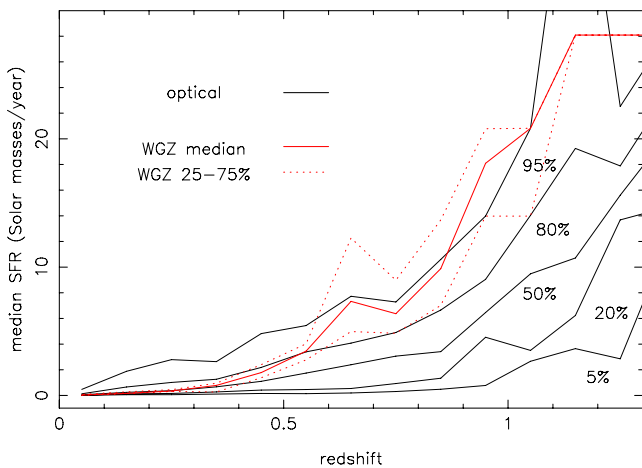
Figure 3. Median SFRs in WiggleZ galaxies compared to optically selected galaxies. The distribution of SFR in WiggleZ galaxies is shown by plotting the median (red line) and the 25th and 75th percentiles (red dotted lines) as a function of redshift. Similarly, the distribution of SFR in the optical reference galaxies is plotted as percentiles (5th to 95th; solid lines) against redshift. The SFR values are not corrected for internal dust extinction (see the text). At redshifts $z > 0.6$, the median SFRs of WiggleZ galaxies put them in the top 5 per cent of optical galaxies by SFR. Note that the WGZ 75th percentile merges into the 50th percentile at $z > 1$.

Figure 4. Detection rate of NUV < 22.8 starburst (SFR > 30 $M_\odot$ yr^{-1}) galaxies in the WiggleZ sample. Insignificant numbers of starburst galaxies are detected at redshifts lower than shown in the plot.

for all galaxies before applying the starburst criterion.[1] The fraction of NUV < 22.8 starburst galaxies that are WiggleZ galaxies were calculated at each redshift[2] using the spectroscopic completeness weights determined above.

The results, in Fig. 4, show that the WiggleZ sample selects about 50 per cent of the NUV < 22.8 starburst galaxy population over the redshift range $0.6 < z < 0.9$. Based on Fig. 3 we might expect the fraction of starburst galaxies to be even higher. This is because the interquartile range of the WiggleZ galaxy SFRs in Fig. 3 straddles the 95th percentile of DEEP2 galaxy SFRs for $z > 0.6$. The 50 per cent detection rate is due to the photometric uncertainty and incompleteness of the *GALEX* MIS photometry. Inspection of the NUV < 22.8 starburst galaxies showed that virtually all of them are selected as a WiggleZ galaxy using the photometry of at least one *GALEX* MIS observation, but only ∼50 per cent are selected using any single observation. This explains the difference between the results in Fig. 4 and our initial expectations of higher completeness rates, which were based on the SFR distributions in Fig. 3.

If we use *r*-band luminosity as a proxy for stellar mass, it is reasonable to assume from Fig. 1 that our sample contains the most massive, $0.6 < z < 0.9$, NUV < 22.8 starburst galaxies within the sample volume. If there were more massive, $0.6 < z < 0.9$, NUV < 22.8 starburst galaxies, then there would not be a dearth of $M_r < -22$ galaxies within the survey selection limits in Fig. 1. This is particularly telling us that the missing $0.6 < z < 0.9$, $M_r < -22$,

NUV < 22.8 starburst galaxies are much more likely to make it into our sample than the $M_r > -22$, $0.6 < z < 0.9$, NUV < 22.8 galaxies. We can apply similar reasoning to the combination of Figs 1 and 2, and argue that our sample is representative of the SFRs of $0.6 < z < 0.9$, NUV < 22.8 starburst galaxies.

We compare the $0.6 < z < 0.9$, NUV < 22.8 starburst galaxy sample to LIRGs, to put them and WiggleZ starburst galaxies into proper context. We have already found that the SFRs of $0.6 < z < 0.9$, NUV < 22.8 starburst galaxies (and WiggleZ starburst galaxies) are consistent with LIRG SFRs. Here we compare the population counts. We calculate the expected number of $0.6 < z < 0.9$, $R < 22.5$ LIRGs using the evolving IR LF in Le Floc'h et al. (2005). We numerically integrate this evolving IR LF over IR luminosities of 10^{11}–$10^{11.4}$ and redshifts of $0.6 < z < 0.9$. The integration is stopped at an IR luminosity of $10^{11.4}$ instead of the LIRG definition of 10^{12}, because this approximates an $R < 22.5$ cut (see fig. 15 of Le Floc'h et al. 2005). We find that $0.6 < z < 0.9$, NUV < 22.8 starburst galaxies constitute ∼7 per cent of the $0.6 < z < 0.9$, $R < 22.5$ LIRG population. When we relax the $R < 22.5$ cut, this becomes ∼6 per cent. UV-luminous starburst galaxies are an appreciable, but minor, component of the entire $0.6 < z < 0.9$, $R < 22.5$ starburst galaxy population (assuming that they are all LIRGs).

4 THE LF OF WiggleZ GALAXIES

We calculated the LF using the Schmidt–Eales (Schmidt 1968; Felten 1976; Eales 1993) estimator, hereafter referred to as the $1/V_{\mathrm{MAX}}$ estimator, with some modifications to include our selection function. In the simple case of N galaxies where each galaxy has completeness C_i and maximum observable volume $V_{\mathrm{MAX}i}$, the LF at luminosity M is

$$\Phi(M) = \sum_{i=1}^{N} 1/(C_i V_{\mathrm{MAX},i})$$

(e.g. Wyder et al. 2005).

---

[1] The choice of global dust correction effectively determines the DEEP2 NUV < 22.8 starburst galaxies when combined with the SFR > 30 $M_\odot$ yr^{-1} criterion. As seen in Fig. 3, WiggleZ galaxies trace the upper envelope of DEEP2 SFRs. For this reason, we use the median of the individual WiggleZ dust corrections to define the DEEP2 NUV < 22.8 starburst sample. This global dust correction is too small for the most highly star-forming DEEP2 galaxies, but the distribution of SFRs within the sample is irrelevant for this particular analysis.

[2] There were insufficient numbers of starburst galaxies in the samples to calculate the fractions at redshifts below $z = 0.6$.
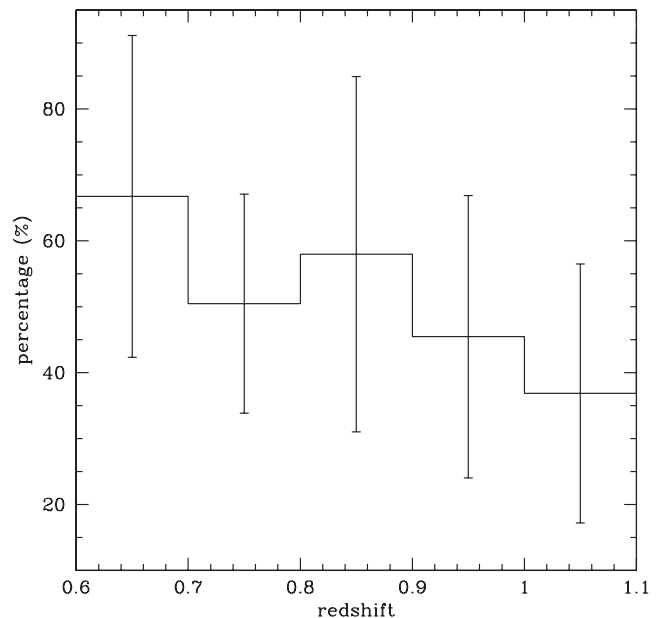
For the WiggleZ survey, we allow the completeness to vary with redshift and position on the sky by writing

$$\Phi(M) = \sum_{i=1}^{N} 1 / \left(\sum_{j=1}^{M} \int_{z\mathrm{min},i}^{z\mathrm{max},i} C_{ij}(z) \mathrm{d}V(z, A_j) \right).$$

The redshift limits $z\mathrm{min}, i$ and $z\mathrm{max}, i$ correspond to the redshift range over which a galaxy satisfies the survey selection criteria (limits in NUV, r, NUV $- r$ and the LRR colour cuts; see Table 2). We split the full survey into M small regions of sky (based on the *GALEX* tiles[3]) over which the completeness does not vary with position. The volume element in each region of area A_j, between redshifts z and $z + \mathrm{d}z$, is then $\mathrm{d}V(z, A_j)$. Dust corrections were not incorporated into the selection function, because we used dust-corrected photometry (corrected using local dust corrections) to create the WiggleZ sample.

The completeness $C_{ij}(z)$ of galaxy i in the survey at a given redshift and position on the sky is the product of terms describing the input catalogues, spectroscopic observations and the use of aperture photometry for the FUV magnitudes,

$$C_{ij}(z) = C_{\mathrm{NUV},i,j}(z) C_{r,i,j}(z) C_{\mathrm{spec},i,j}(z) C_{\mathrm{FUVap},i,j}(z).$$

The terms $C_{\mathrm{NUV},i,j}$ and $C_{r,i,j}$ describe the completeness of the *GALEX* MIS and SDSS photometry, respectively. The probability that a redshift is obtained for this galaxy via spectroscopic observation is encapsulated by the term, $C_{\mathrm{spec},i,j}$. The final term, $C_{\mathrm{FUVap},i,j}$, is an effective completeness, describing the probability that the FUV $-$ NUV colour criterion is satisfied. We assume that these components are independent and separable. Each of these terms and the methods we used to measure them is described in detail in Appendix C.

The summation of $1/V_{\mathrm{MAX}}$ values measures the integrated LF, $\Phi(M)$. The differential LF, $\phi(M)$, is the integrated LF dividing by the magnitude interval used to bin galaxies when summing $1/V_{\mathrm{MAX}}$ values. We note that it is important to explicitly account for the survey selection boundaries in redshift–luminosity space when converting $\Phi(M)$ to $\phi(M)$. The survey selection boundaries reduce the effective magnitude interval of the brightest and faintest magnitude bins at all redshifts. In practice, only the faintest galaxies at every redshift are affected. This is because only the faintest galaxies in our sample met the survey selection limits in redshift–luminosity space (see Fig. 1). At all redshifts, the LF of the faintest galaxies appeared erroneously low when the selection boundaries in redshift–luminosity space were neglected.

We calculated uncertainties in the individual V_{MAX} values by propagating the uncertainties in the survey window function and selection function, and then allowing for discretization of the redshift values used to measure the observable redshift ranges. We used bootstrap resampling to estimate the effect of outliers on the LF measurements. A small number of extremely small or large V_{MAX} values can distort the LF measurements, because it is a summation of $1/V_{\mathrm{MAX}}$ values. We present an analysis of the reliability of our V_{MAX} measurements in Appendix D1.

We present the resulting NUV LFs in 16 redshift bins in Fig. 5. We also calculated the LFs with a correction for the LRR cuts. Using WiggleZ data taken prior to the inclusion of the LRR cuts, we measured the fraction of galaxies that are removed by them in r magnitude–redshift space (described in full in Appendix D2).

---

[3] We used Voronoi (1908) tessellation on the *GALEX* tile centres to define a unique region of sky that belongs to each tile.

The LRR corrections are the inverses of these fractions. The LRR-corrected LFs are shown in Fig. D5. We also calculated r-band optical LFs without and with the LRR corrections; these are shown in Figs D6 and D7. The numerical values and uncertainties for all the LFs are given in Appendix D4.

4.1 Schechter function fits

We fitted Schechter functions to all the LFs using the Levenberg–Marquardt method of non-linear χ^2 minimization. This method provides uncertainties for each of the parameters through a full covariance matrix. We excluded the brightest magnitude bin from each fit to minimize the effect of any remaining quasars in our sample, and account for the fact that the Schechter function is known to deviate from measured LFs at the brightest magnitudes (Schechter 1976). At higher redshifts, the WiggleZ data do not contain any information about the faint-end slope, α, because of the small luminosity range sampled. We accounted for this by keeping α fixed. We used α values of -0.5, -1, -1.5 and -2 to span the range of α values in the literature (e.g. Arnouts et al. 2005; Treyer et al. 2005). We only fitted the normalization, $\phi*$, and the position of the 'knee' in the LF, $M*$.

The resulting Schechter functions are plotted over the LFs in Figs 5, D5, D6 and D7. We also plot vertical lines marking the value of $M*$ according to the different slopes used. The Schechter functions match the data well over the luminosities fitted, independent of the value assumed for α and the application of an LRR cut correction. The reduced χ^2 for all of these fits is of order 1. The one exception is that fits to the LRR-corrected, $z < 0.55$ optical data only converge for $\alpha = -0.5$. The Schechter function does not fit the data well at the bright end of the LFs. The NUV data are systematically higher than the Schechter fits at luminosities above $M_{\mathrm{NUV}} \approx -21.5$. The r-band LFs do not present such pronounced deviations from the Schechter function, but this may be because we are not sampling luminosities greater than $M*$ in the r-band data (see Fig. 1). We discuss possible explanations for the deviation in the next section. The Schechter function parameter values and the reduced χ^2 values for the NUV and r LFs are presented in Appendix D4.

The $M*$ values for the $\alpha = -1$ fits are overlaid on the WiggleZ galaxies and selection boundaries in Fig. 1. Consistent with our earlier analysis in Section 3, in Fig. 1 the WiggleZ galaxies transition from $\sim M_{\mathrm{NUV}}*$ to brighter than $M_{\mathrm{NUV}}*$ UV galaxies at $z = 0.6$. At the same redshift, WiggleZ galaxies transition from fainter than M_r* to $\sim M_r*$ optical galaxies. As the WiggleZ sample is a good tracer of the highly star-forming galaxy population, this implies that at these redshifts ($0.6 < z < 0.9$) the majority of highly star-forming UV-luminous galaxies are luminous M_r* optical galaxies.

Although our individual LF measurements are accurate, the luminosity range is too small to put strong constraints on all three Schechter function parameters. The joint confidence intervals in $M*$ and $\phi*$ in Fig. 6 exhibit significant degeneracy between the two parameters at each redshift.

Fig. 6 shows how the fitted LF parameters evolve as redshift increases from left to right. The fits to the uncorrected LFs (solid curves) show a rapid increase in $M*$ luminosity over the redshift range $0.1 < z < 0.5$ values (black then red curves). However, the fits to the corrected functions (dotted curves) show less change, albeit with large uncertainties. Furthermore, the values of $M*$ are also strongly dependent on the faint-end slope for these low-luminosity samples, so we cannot make any firm conclusions about the evolution of the fits at low ($z < 0.5$) redshifts. We do note, however, that
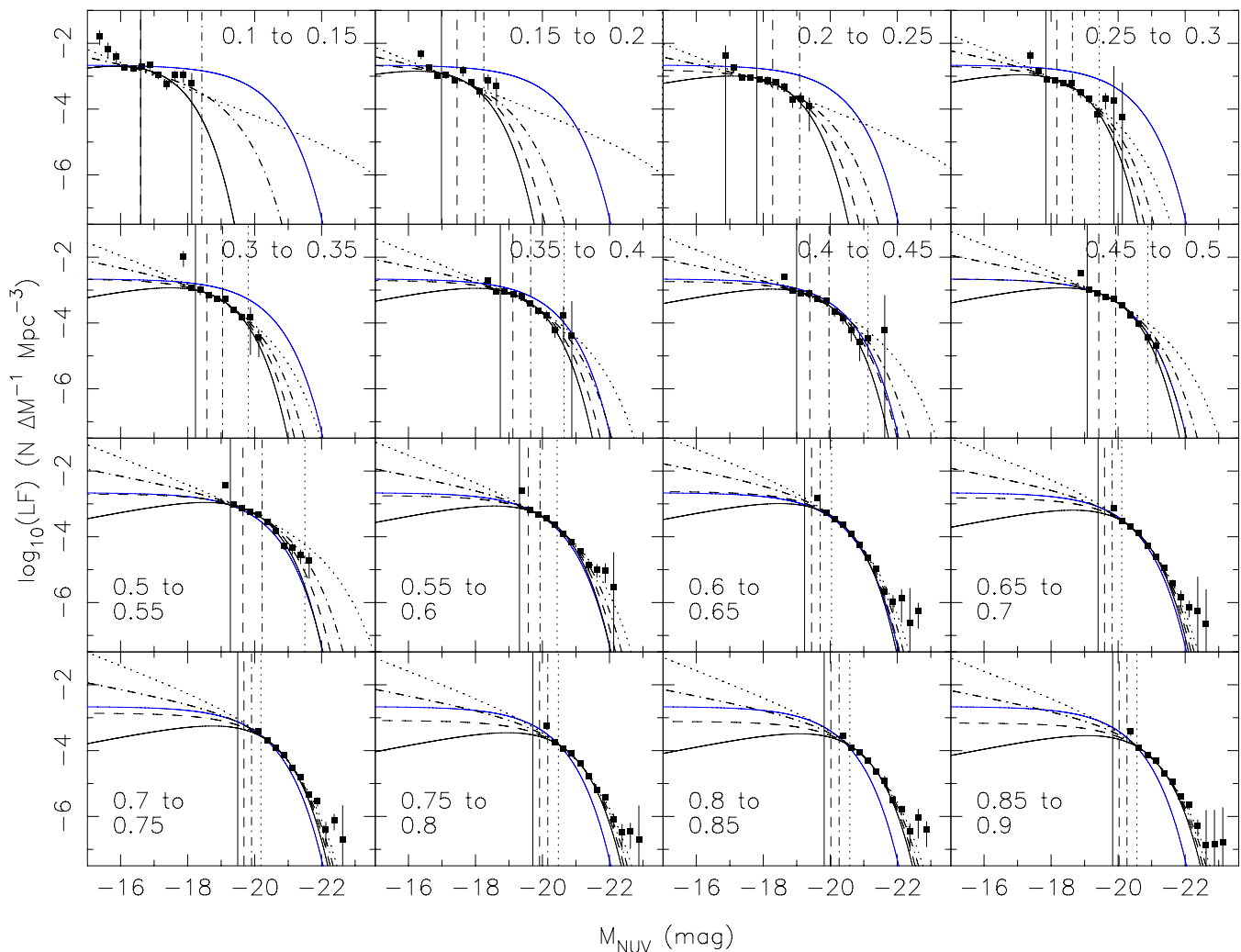
Figure 5. The NUV LFs of WiggleZ galaxies at 16 independent redshifts. The solid, dashed, dot–dashed and dotted lines correspond to Schechter function fits using fixed faint-end slopes of $\alpha = -0.5, -1.0, -1.5$ and -2. The vertical lines indicate the fitted $M*$ parameters for these fits using the same line styles. We can fit Schechter functions that are consistent with our data, but the parameters are poorly constrained. The $\alpha = -1$, $0.4 < z < 0.45$ fit is overplotted in blue as a visual reference.

a similarly rapid change in $M*$ over the same redshift range was reported by Arnouts et al. (2005).

At higher ($z > 0.5$) redshifts (the green and blue curves in Fig. 6), $M*$ increases steadily but less rapidly with redshift and the fits to the raw and corrected LFs are much more consistent. However, we note that the confidence intervals become more elongated at the highest redshifts as there are fewer galaxies to constrain the normalization of the LF. The change in evolution of the fitted parameters around redshift $z = 0.5$ can largely be explained by a change in the galaxy population at these redshifts, as can be seen in Fig. 1.

We also show previous measurements of $M*$ and $\phi*$ from fits to the LF in Fig. 6. The point indicated by a large square is by Budavári et al. (2005) for galaxies selected with NUV < 21.5 at redshift $z = 0.1$. The two points indicated by crosses are by Treyer et al. (2005) for galaxies selected with NUV < 20 at redshifts $z = 0.05$ and 0.15. The circles are by Arnouts et al. (2005) for galaxies selected with NUV < 24.5. In each case, we have used the values for blue (late-type) galaxies in their samples to best correspond to the WiggleZ galaxies. The previous measurements are generally consistent with the WiggleZ measurements apart from the second value (at $0.1 < z < 0.2$) by Treyer et al. (2005) at $(M*, \log \Phi) =$

$(-18.7, -2.8)$ which has a normalization Φ below the WiggleZ value. This difference may be explained by the different populations sampled by the two surveys at this redshift. The sample in Treyer et al. (2005) has an NUV magnitude limit 2.8 mag brighter than that of WiggleZ and 1.5 mag brighter than the $0.07 < z < 0.25$ sample in Budavári et al. (2005), and does not exclude galaxies with the bluest NUV $- r$ colours as WiggleZ does. Treyer et al. (2005) stated that their $0.1 < z < 0.2$ sample is dominated by bluer galaxies, so it is likely that this sample is dominated by galaxies with higher SFRs than $0.1 < z < 0.2$ WiggleZ galaxies. This may be a contributing factor to the discrepancy in the FUV LFs of Budavári et al. (2005) and Treyer et al. (2005), which was identified in Budavári et al. (2005).

In Fig. 7, we show the evolution of the fitted values of $M*$ over the whole redshift range for both the raw and corrected LFs. The values are consistent at high redshift ($z > 0.5$), but differ at lower redshifts where the LRR correction is being applied. We also note that the fitted value of $M*$ is poorly constrained by our data at lower redshifts: the value is quite sensitive to the faint-end slope α adopted for the fit leading to systematic uncertainties larger than the statistical uncertainties shown in the figure. We therefore restrict
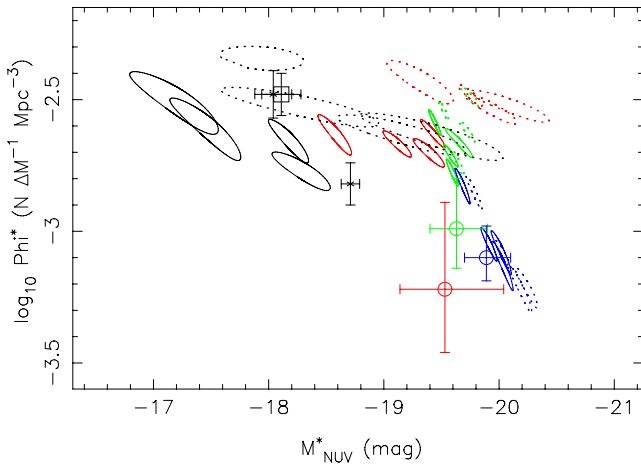
Figure 6. Schechter function fits to the NUV LFs. The ellipses give 68 per cent confidence intervals for M^* and ϕ^*; the faint-end slope was fixed at $\alpha = -1$. The solid curves are for the raw LFs and the dotted curves are for the LRR-corrected LFs, colour coded according to redshift: $0.1 < z < 0.3$ (black), $0.3 < z < 0.5$ (red), $0.5 < z < 0.7$ (green) and $0.7 < z < 0.9$ (blue). The black squares and crosses show values measured by Budavári et al. (2005) and Treyer et al. (2005), respectively; the circles show values from Arnouts et al. (2005), using the same colour coding as for redshift.
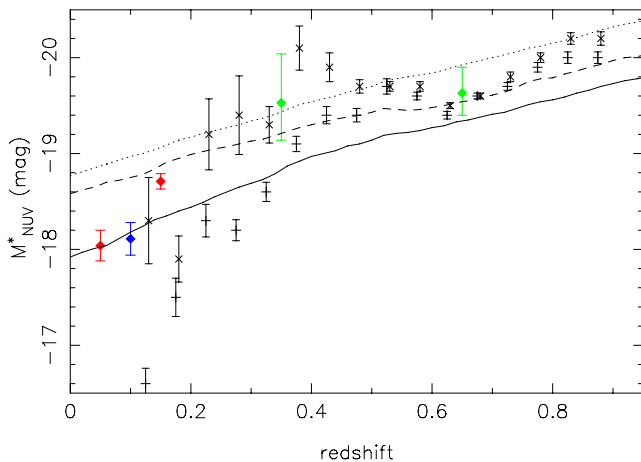

Figure 7. The evolution of M^* with redshift for WiggleZ and other *GALEX* samples. The uncorrected and LRR-corrected WiggleZ M_{FUV}^* values are plotted with $+$ and $\times$ symbols, respectively. The LRR-corrected values are also offset by $+0.005$ in redshift. The Arnouts et al. (2005), Budavári et al. (2005) and Treyer et al. (2005) M_{FUV}^* values are plotted as green, blue and red diamonds. Predictions of M_{1500}^* (Scannapiecoet al. 2005) for AGN feedback equal to 2.5, 5 and 10 per cent of the bolometric luminosity are plotted as dotted, dashed and solid lines.

our discussion to the high-redshift WiggleZ data points. In the high-redshift region, our values of M^* increase as redshift increases. This is consistent with previous reports of strong evolution in M^* (Arnouts et al. 2005; Budavári et al. 2005; Treyer et al. 2005), although we cannot confirm the even more rapid evolution at low redshifts.

The evolution of the characteristic maximum galaxy luminosity (i.e. M^* in Fig. 7) was used by Scannapiecoet al. (2005) to test a model of galaxy formation where star formation is inhibited by energy injected by central black holes ('AGN feedback'), leading to cosmic downsizing, the steady decrease in the size of the most active star-forming galaxies. To test their model, Scannapiecoet al. (2005)

compared the measured M^* values in Arnouts et al. (2005) to their predicted 1500 Å M^*, for various levels of feedback efficiency.[4] We show the evolution in M^* predicted by Scannapiecoet al. (2005) for three different levels of AGN feedback as well as the measurements for blue/early-type galaxies by Arnouts et al. (2005), Budavári et al. (2005) and Treyer et al. (2005).

The WiggleZ measurements (at the reliable redshifts $z > 0.5$) extend the previous comparison to much higher redshift. The WiggleZ measurements are generally consistent with the model predictions. We also observe a potential trend of WiggleZ measurements to evolve quicker than the model predictions. This is most noticeable at $z > 0.6$, where it can be argued that the WiggleZ measurements move from the 2.5 per cent feedback relation at $z = 0.9$ to the 5 per cent feedback relation at $z = 0.6$. The SFRs and stellar masses (using r-band luminosity as a proxy for stellar mass) of WiggleZ galaxies increase with redshift. If the trend in our data is real (evolving from one feedback relation to another), then the Scannapiecoet al. (2005) model would need to explain an AGN feedback efficiency that increases with one or more of the following: time, stellar mass and SFR.

5 DISCUSSION

In this section, we discuss the evolution of the most luminous WiggleZ galaxies, as well as their contribution to the total cosmic SFR. We also examine the deviation of the WiggleZ LFs from a Schechter function at bright magnitudes.

5.1 Evolution of density and SFR density

We analysed a region in redshift–luminosity space that was fully sampled by WiggleZ, i.e. completely within the selection boundaries. In particular, we only used galaxies at redshifts $z \geq 0.6$ to analyse a consistently selected galaxy population and minimize the effects of the LRR cuts. We adopted a luminosity range of $-21 < M_{NUV} < -22.5$ and redshift range $0.6 < z < 0.9$. The lower luminosity limit approximately corresponds to an SFR of $30\,M_\odot\,yr^{-1}$ so these galaxies are all starburst galaxies. We modelled the evolution of each sample by fitting the power-law index γ to functions of the form $(1 + z)^\gamma$ to the comoving number and star formation densities. We repeated the analysis on the galaxy numbers with the LRR correction applied. We plot the number density and star formation density values as a function of redshift in Fig. 8 and list the fitted power laws in Table 4.

The luminous WiggleZ galaxies show a rapid evolution in both number density: $\gamma = 6.5 \pm 0.9$, and SFR density: $\gamma = 5.4 \pm 0.9$. The evolution is slightly slower when corrected for the LRR cuts: this is as expected because the correction increases the number of galaxies at $z < 0.6$. This evolution is much more rapid than observed in normal galaxies (e.g. $\gamma \approx 2.5$; Hopkins 2004). As we noted in the introduction however, UV-luminous galaxies are known to evolve faster, with $\gamma \approx 5$ for the $M_{FUV} < -19.3$ ($M_{NUV} < -19.5$) galaxies measured by Schiminovich et al. (2005). Our results show that this trend continues to even more luminous galaxies: the WiggleZ galaxies have luminosities brighter by a magnitude or more. We expect the most UV-luminous galaxies in our sample to be the most massive, because of the $NUV - r$ colour cuts. At these redshifts, the most massive star-forming galaxies in our sample therefore exhibit the fastest decline in SFR with time: in Section 5.2 below

---

[4] Scannapiecoet al. (2005) denote the fraction of the total AGN energy injected as kinetic energy as ϵ_k which they vary from 2.5 to 10 per cent.
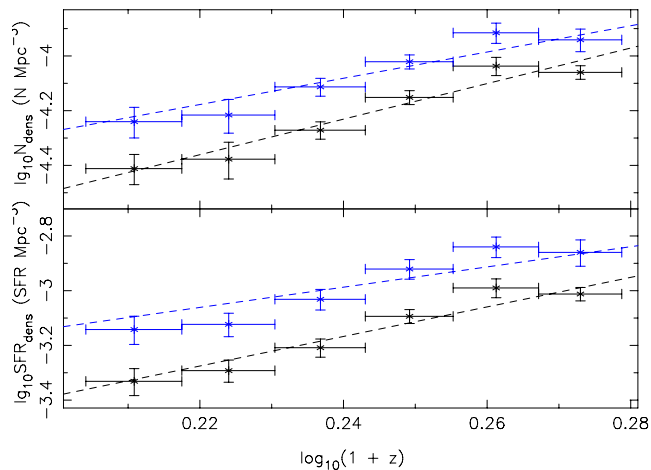
Figure 8. Evolution of number density (upper panel) and star formation density (lower panel) of luminous WiggleZ galaxies. These are calculated over the luminosity ($-21 < M_{NUV} < -22.5$) and redshift ($0.6 < z < 0.9$) ranges completely sampled by the survey. In each panel, the upper (blue) points are corrected for the galaxies removed by the LRR colour limits. The fits in Table 4 are plotted with dashed lines in both panels.

Table 4. Evolution of luminous WiggleZ galaxies.

Sample	LRR corrected	γ_N	γ_{SFR}
$-21 < M_{NUV} < -22.5$	No	6.5 ± 0.9	5.4 ± 0.9
$-21 < M_{NUV} < -22.5$	Yes	4.8 ± 1.2	3.7 ± 1.3

Note: for each sample, the evolution was fitted by a function of the form $(1 + z)^\gamma$ to the number density or star formation density. This was calculated at redshifts fully sampled by the survey at these luminosities: $0.6 < z < 0.9$.

we examine the contribution of these extreme galaxies to the total SFR of the Universe.

5.2 Contribution of luminous galaxies to total cosmic star formation density

In Fig. 9, we compare the contribution of the luminous WiggleZ galaxies (described in the previous section) and the full WiggleZ sample to the total cosmic SFR density. Both samples have been corrected for the LRR cuts. We also show in the same figure a parametrized measurement of the cosmic SFR density from Hopkins & Beacom (2006). Note that we first apply a scale factor of 2.0 (Hopkins & Beacom 2006) to correct the total SFR density from the Baldry & Glazebrook (2003) initial mass function (IMF) used by Hopkins & Beacom (2006) to the Salpeter (1955) IMF used in this paper. The fractional contribution of the WiggleZ samples to the total SFR is shown in the lower panel of Fig. 9.

The SFR density and fractional contribution of the full WiggleZ sample peak with a 40 per cent contribution at a redshift of $z = 0.4$. (Similar evolution is observed in the uncorrected WiggleZ sample, but the contribution to the total cosmic SFR density peaks at $\sim$11 per cent around $z \sim 0.4$.) The peak occurs because this is the redshift at which the WiggleZ galaxies best sample the $M_{NUV}*$ region of the LF that contributes most to the integrated SFR. In contrast, in the optical r band, the WiggleZ galaxies at this redshift are all less luminous than M_r*, peaking at about $M_r*+1.5$ (see the lower panel of Fig. 1). This means that at least 40 per cent of all star
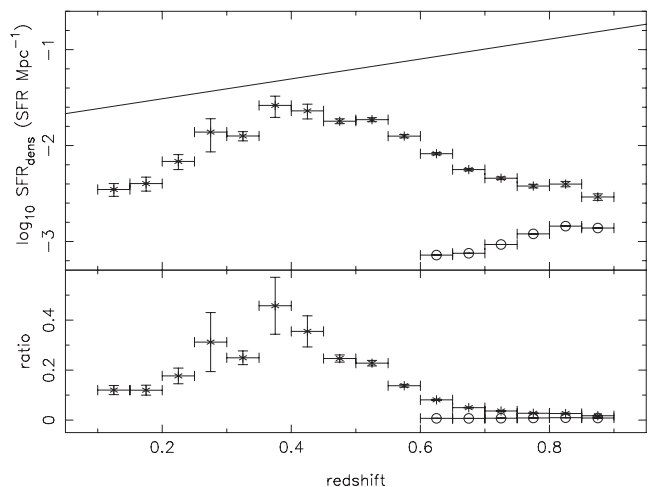

Figure 9. The contribution of all WiggleZ and WiggleZ starburst galaxies to the total cosmic SFR density as a function of redshift. Top panel: the SFR density of all WiggleZ galaxies (asterisks) and WiggleZ starburst galaxies (circles). The solid curve indicates the total cosmic star formation density estimated by Hopkins & Beacom (2006). Bottom panel: the fraction of the cosmic SFR density contributed by all WiggleZ (asterisks) and WiggleZ starburst galaxies (circles).

formation is taking place in galaxies less luminous than M_r* by a redshift of $z = 0.4$.

The fractional contribution of the luminous ($-21 < M_{NUV} < -22.5$, starburst) WiggleZ galaxies to the cosmic SFR density is almost constant over this redshift range $0.6 < z < 0.9$, at about 1 per cent of the total density estimated by Hopkins & Beacom (2006). This value is consistent with the earlier measurements by Schiminovich et al. (2005, their fig. 5). We measure an LRR-corrected SFR density of $10^{-3.25 \pm 0.05}$ M$_\odot$ yr^{-1}Mpc^{-3} for our starburst galaxies at $z = 0.875$, after removing the $\sim$0.9 mag dust correction applied to the values in Fig. 9. The corresponding total SFR density measured by Schiminovich et al. (2005) at $z = 0.9$ from $M_{FUV} < -19.32$ galaxies is $\log(\rho*) = -2.31^{+0.3}_{-0.15}$ M$_\odot$ yr^{-1}Mpc^{-3} (correcting for the 25 per cent of the total contributed by these galaxies, but not correcting for internal dust). The discrepancy between the SFR densities can be attributed to our brighter sample, as their sample includes $\sim M_{FUV}*$ at $z = 0.9$, but WiggleZ galaxies are brighter than $M_{FUV}*$ at this redshift.

Our key result from this section is that we have been able to separate the contribution of the most UV-luminous galaxies ($-21 < M_{NUV} < -22.5$) to total cosmic SFR density for the first time. The contribution of these galaxies to the total SFR density is around 1 per cent over the redshifts we studied ($0.6 < z < 0.9$). We expect that these galaxies are also the most massive galaxies in our sample (due to the NUV $- r$ colour cuts), and that they are the most massive, UV-luminous, $0.6 < z < 0.9$ starburst galaxies (using survey selection limit arguments and M_r as a stellar mass proxy). This confirms the prediction we make in the introduction that the most massive, UV-luminous galaxies should have formed the bulk of their stars before a redshift of $z \approx 1$.

Our results are consistent with previous observations of the contribution of IR-luminous galaxies to the Universe SFR density. Le Floc'h et al. (2005) found that LIRGs contribute at least 50 per cent of the Universe SFR density at $z \sim 1$. This was confirmed by subsequent analyses in Caputi et al. (2007) and Magnelli et al. (2009). All three also observed that the dominant contribution to the Universe SFR density transitioned from quiescently star-forming galaxies to
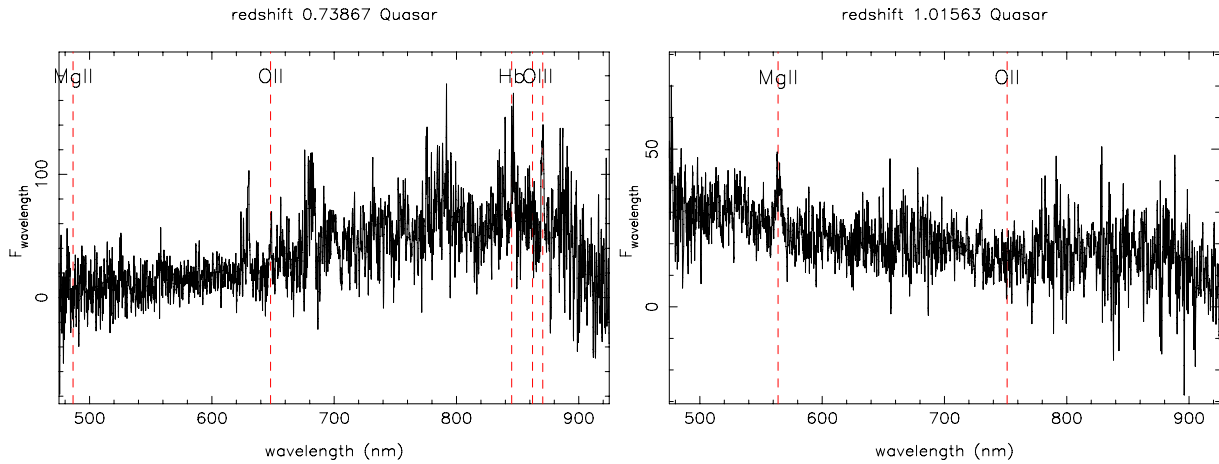
Figure 10. Spectra of $z = 0.74$ and 1.02 quasars in the WiggleZ sample with emission lines marked. The spectra have been 5σ clipped and smoothed by taking the mean of a 5 pixel sliding boxcar. The $z = 0.74$ spectrum illustrates the difficulty in classifying quasars at lower redshifts when the characteristic UV lines (e.g. Mg ɪɪ) are not visible in the spectra.

LIRGs between $z = 0.7$ and 0.9. These previous observations are consistent with both the declining contribution of WiggleZ galaxies to the Universe SFR density from $z = 0.4$, and the negligible contribution of UV-luminous starburst galaxies at $z \sim 1$.

Models of IR-luminous galaxy contribution to the Universe SFR density are also consistent with our results. Models in Hopkins et al. (2010) and Sargent et al. (2012), which were tested against observed IR LFs, demonstrated that $z < 1$ LIRGs are predominantly powered by quiescent star formation. They also showed that starbursts contribute $\sim$10 per cent of the Universe SFR density at $z \sim 1$, declining to $\sim$5 per cent at $z = 0$. The contribution of UV-luminous starburst galaxies that we measure is well within these model predictions. These results are consistent with our finding (see Section 3) that UV-luminous starburst galaxies are an appreciable ($\sim$7 per cent), but minor, component of the entire starburst galaxy population at $0.6 < z < 0.9$.

5.3 Bright end of the LFs

The NUV LFs in Fig. 5 deviate from the Schechter function fits at the bright end. In this section, we examine the cause of these deviations and derive an analytic description of the high-luminosity behaviour of the LFs.

We first re-examined the spectra of the most luminous WiggleZ galaxies. At the redshifts where significant deviations from the Schechter function fit were evident ($0.6 < z < 0.9$), we selected the galaxies within 0.5 mag of the most luminous, giving a sample of 99 spectra. Approximately a third had broad ($\geq$1000 km s^{-1}) lines indicating quasars or AGN and the rest were emission line galaxies. This shows that not all quasars were identified by inspection of the spectra (and removed from our sample). We note that the identification of quasars in this way was not intended to be complete. At high redshifts ($z > 0.75$), the quasar UV rest-wavelength lines (Mg ɪɪ at 2798 Åand the bluer lines) are relatively easy to identify as having broad components in our low signal-to-noise spectra. By contrast, quasars at lower redshifts ($z < 0.75$) are only identifiable if they have sufficiently good spectra that a broadening of the Hβ line can be identified. This is demonstrated in Fig. 10, where the spectra of $z \sim 0.75$ and $z \sim 1$ quasars in the WiggleZ sample are plotted. We expect the manual identification rate of quasars in our sample from emission lines to increase with redshift. We also expect the number density of quasars to increase with redshift. Combining geomet-

ric projection effects with increasing quasar density and increasing quasar identification rates, we expect quasar contamination to occur over $0.5 < z < 0.9$.

Given the difficulty of removing all quasars based on the WiggleZ spectra, we instead measured any residual quasar contributions to the LFs by fitting a modified Schechter function, with extra contributions from both quasars and a possible power-law extension at high luminosities.

For the quasar contribution, we calculated the quasar NUV LF using the *qlf_calculator* code (Hopkins, Richards & Hernquist 2007). This code calculates the monochromatic $d\Phi/d(\log_{10}L)$ LF in AB magnitudes at a given redshift and observing frequency. We calculated the central frequency of the *GALEX* NUV filter to be 1.2946×10^{15} Hz, and then scaled the output by 0.4 to obtain the $d\Phi/dM$ LF used here. We allowed the fraction of the quasar LF contributing to the WiggleZ counts to vary as a free parameter.

The quasar LF is not necessarily representative of the quasar contribution. For example, the fraction of the quasar LF that contributes to the WiggleZ LF may vary with luminosity. Fortunately, the WiggleZ LF was calculated using the $1/V_{MAX}$ estimator. This means that any luminosity-dependent contribution of the quasar LF is averaged over bins of 0.5 mag. Similarly, we are fortunate that the WiggleZ LF is orders of magnitude larger than the quasar LF until the very brightest luminosities. This means that the quasar contribution is only of concern for the few brightest magnitude bins. Taking into account both effects, we expect a scaled quasar LF to be a good first-order approximation of the actual quasar contribution to the WiggleZ LF.

For the high-luminosity extension, we replaced the normal Schechter function with a power-law term of the form $\Phi = 10^{\gamma M + \theta}$ at luminosities above a 'break' luminosity L_0. We required that the power law match the slope of the normal function at the transition luminosity, so L_0 was the only free parameter in this extra component.

We found the best-fitting model for each LF out of the following possibilities: pure Schechter function, pure Schechter function + quasar LF, extended Schechter function and extended Schechter function + quasar LF. We tested a range of break luminosities L_0 and scalings of the quasar NUV LF. The best-fitting model for each LF according to χ^2 minimization is shown in Fig. 11. Note that a more complex model was only chosen if the penalty (measured with the Akaike information criterion, AIC; Akaike 1974) associated
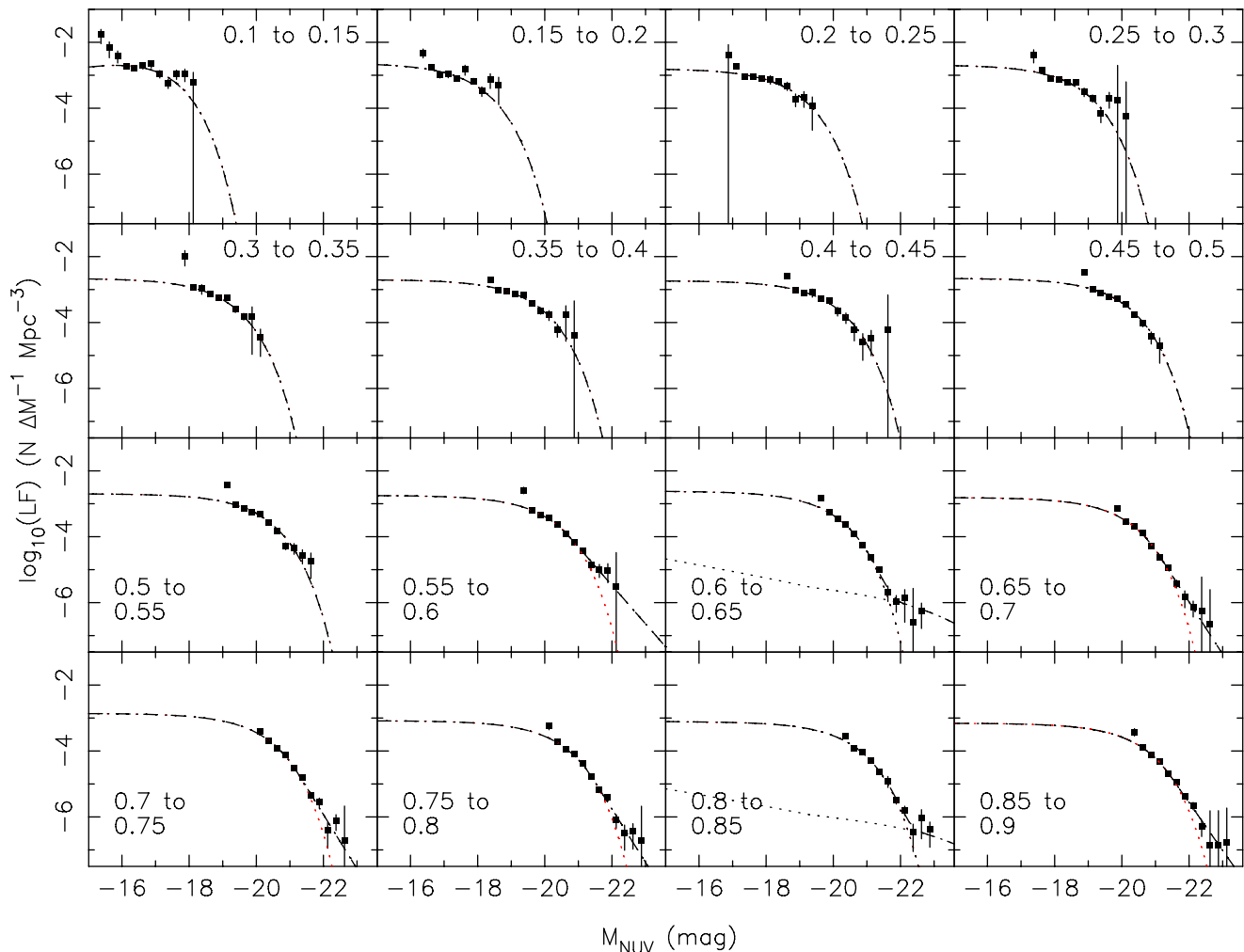
Figure 11. NUV LF fits with extra high-luminosity contributions. The measured LF (square points) at each redshift is shown with the original Schechter function fit (red dotted lines), predicted QSO NUV LF (nearly horizontal dotted line), Schechter-into-power-law analytic model (curving dashed line with high density at faint luminosities) and the sum of the QSO LF and analytic model (dashed lines). The quasar contribution is only required at two redshifts.

with increasing the number of free parameters is offset by the improvement to the χ^2 value of the fit.

At all redshifts above $z = 0.55$, the best-fitting models in Fig. 11 required the extended Schechter function. Somewhat surprisingly, in only two cases ($0.6 < z < 0.65$ and $0.8 < z < 0.85$) was a contribution from the quasar LF also justified. At these redshifts, the quasar contribution is probably real and the scalings of 0.5 ± 0.17 ($0.6 < z < 0.65$) and 0.17 ± 0.08 ($0.8 < z < 0.85$) correspond to a significant fraction of the quasar population. Applying the LRR corrections does not significantly alter the need for a quasar contribution at these redshifts. A quasar contribution is still required for the $0.6 < z < 0.65$ LRR-corrected NUV LF. It is also required initially for the $0.8 < z < 0.85$ LRR-corrected NUV LF, but is marginally rejected after applying the AIC penalty.

When we analyse the final WiggleZ survey data, we will obtain precise LFs that extend to brighter luminosities. The selection boundaries of the WiggleZ survey in Fig. 1 show that the complete WiggleZ sample has the potential to extend the LFs by half a magnitude at $z \sim 0.6$ or 1.5 mag at $z \sim 0.9$. This will allow us to repeat this analysis and improve our characterization of the bright end as a combination of residual quasar contamination and intrinsic deviation.

6 CONCLUSIONS

We have used the WiggleZ Dark Energy Survey to measure the properties of UV-luminous galaxies at redshifts up to $z = 0.9$. We demonstrated that the WiggleZ galaxies reliably trace the starburst galaxy population over the range $0.6 < z < 0.9$. We constructed LFs of the WiggleZ galaxies and determined their contribution to the total cosmic SFR density. The details of these results are as follows.

(i) We have characterized the properties of galaxies selected for the WiggleZ survey by comparison with a deep optical reference sample. We found that WiggleZ selects 1.76 ± 0.05 per cent of all $0.1 < z < 0.9$, $R < 22.5$ optically selected galaxies and 10.1 ± 0.3 per cent of all $0.1 < z < 0.9$, $R < 22.5$, NUV < 22.8 UV-selected galaxies. The median SFR of WiggleZ galaxies sits on the 50th percentile for optically selected galaxies at $z \leq 0.3$. The median WiggleZ SFR moves to higher percentiles at higher redshifts, until at $z > 0.6$, WiggleZ galaxies have a median SFR in the 95th percentile. If we define starburst galaxies as those having SFR $> 30 \, M_\odot \, yr^{-1}$ (Cowie et al. 1996), then the WiggleZ selection criteria should include all NUV < 22.8 starburst galaxies at redshifts above $z = 0.6$. We showed that the WiggleZ sample contains approximately 50 per cent of the $0.6 < z < 0.9$, NUV < 22.8 starburst galaxy

population in our sample volume, consistent with the observational completeness at these magnitudes.

(ii) We measured the maximum observable volumes, V_{MAX}, for 39 966 galaxies from the first public data release (DR1) of the WiggleZ survey. Using these V_{MAX} values, we constructed LFs for the WiggleZ galaxies in the *GALEX* NUV and the SDSS *r* bands.

(iii) Our large sample size allowed us to separate the contribution of the most UV-luminous ($-21.5 < M_{NUV} < -22.5$, i.e. starburst) galaxies to the total cosmic star formation. These galaxies have a measured SFR density of $10^{-2.7}\,M_{\odot}\,yr^{-1}\,Mpc^{-3}$ and it evolves as $\Phi \propto (1 + z)^{5\pm1}$, consistent with the trends seen in the previous analysis of a smaller sample (Schiminovich et al. 2005). We showed that the contribution of these galaxies to the total cosmic SFR density is already less than 1 per cent of the total at a redshift of $z = 0.9$ and that it remains at this low level over the redshift range measured ($0.6 < z < 0.9$). This confirms the expectation (Arnouts et al. 2005) that the majority of massive galaxies will have formed the bulk of their stars before a redshift of $z \approx 1$. The negligible contribution of UV-luminous starburst galaxies to the Universe SFR density is also consistent with previous observations and model predictions: Le Floc'h et al. (2005), Caputi et al. (2007) and Magnelli et al. (2009) found that LIRGs contribute the bulk of the Universe star formation at $z \sim 1$; we found that UV-luminous starburst galaxies constitute ~7 per cent of the entire starburst galaxy population; models in Hopkins et al. (2010) and Sargent et al. (2012) predict a starburst galaxy contribution of ~10 per cent at $z \sim 1$.

(iv) We derived analytic fits to the LFs by extending the functional form of the Schechter function and including a contribution from quasars. We extended the Schechter function by having it smoothly transition to a power-law form at high luminosities. We included a possible contribution from quasars, due to residual quasar contamination of our sample. We selected the best-fitting model for each LF using χ^2 minimization. These fits showed that the extended Schechter function is a better fit than the traditional Schechter function for most redshifts in the range $0.55 < z < 0.9$; there is also evidence of residual quasar contamination for $0.6 < z < 0.65$ and $0.8 < z < 0.85$.

(v) The analytic fits to the LFs can be used to measure the radial selection function of the WiggleZ survey or test models of galaxy formation and evolution. In this paper, we compared the analytic fits to predictions for an AGN feedback model in Scannapieco et al. (2005). The WiggleZ $M*_{NUV}$ values are consistent with the models in Scannapieco et al. (2005). We also note a potential evolution in the WiggleZ $M*_{NUV}$ values that is faster (with redshift) than predicted in Scannapieco et al. (2005). If this trend in our data is real, the AGN feedback efficiency needs to increase (over $0.1 < z < 0.9$) with one or more of the following: time, stellar mass and SFR.

NOTE ADDED IN PRESS

An explanation for an intrinisic LF excess in the UV has been posited in Salim & Lee (2012). Their model of SFR based (UV) LFs derived from specific SFRs and mass based (optical/IR) LFs predicts an intrinic excess.

REFERENCES

Adelman-McCarthy J. K. et al., 2006, ApJS, 162, 38
Akaike H., 1974, IEEE Trans. Autom. Control, 19, 716
Arnouts S. et al., 2005, ApJ, 619, L43
Avni Y., Bahcall J. N., 1980, ApJ, 235, 694
Baldry I. K., Glazebrook K., 2003, ApJ, 593, 258
Bell E. F., 2002, ApJ, 577, 150
Blake C. et al., 2009, MNRAS, 395, 240
Blanton M. R., Roweis S., 2007, AJ, 133, 734
Brown M. J. I., Dey A., Jannuzi B. T., Brand K., Benson A. J., Brodwin M., Croton D. J., Eisenhardt P. R., 2007, ApJ, 654, 858
Buat V., Xu C., 1996, A&A, 306, 61
Budavári T. et al., 2005, ApJ, 619, L31
Calzetti D., Kinney A. L., Storchi-Bergmann T., 1994, ApJ, 429, 582
Calzetti D., Armus L., Bohlin R. C., Kinney A. L., Koornneef J., Storchi-Bergmann T., 2000, ApJ, 533, 682
Caputi K. I. et al., 2007, ApJ, 660, 97
Coil A. L., Newman J. A., Kaiser N., Davis M., Ma C.-P., Kocevski D. D., Koo D. C., 2004, ApJ, 617, 765
Cortese L., Boselli A., Franzetti P., Decarli R., Gavazzi G., Boissier S., Buat V., 2008, MNRAS, 386, 1157
Cowie L. L., Songaila A., Hu E. M., Cohen J. G., 1996, AJ, 112, 839
Davis M. et al., 2003, Proc. SPIE, 4834, 161
Davis M. et al., 2007, ApJ, 660, L1
Drinkwater M. J. et al., 2010, MNRAS, 401, 1429
Eales S., 1993, ApJ, 404, 51
Felten J. E., 1976, ApJ, 207, 700
Gallego J., Zamorano J., Aragon-Salamanca A., Rego M., 1995, ApJ, 455, L1
Hopkins A. M., 2004, ApJ, 615, 209
Hopkins A. M., Beacom J. F., 2006, ApJ, 651, 142
Hopkins P. F., Richards G. T., Hernquist L., 2007, ApJ, 654, 731
Hopkins P. F., Younger J. D., Hayward C. C., Narayanan D., Hernquist L., 2010, MNRAS, 402, 1693
Kennicutt R. C., Jr, 1998, ARA&A, 36, 189
Le Floc'h E. et al., 2005, ApJ, 632, 169

Levenberg K., 1944, Q. Appl. Math., 2, 164

Magnelli B., Elbaz D., Chary R. R., Dickinson M., Le Borgne D., Frayer D. T., Willmer C. N. A., 2009, A&A, 496, 57

Marquardt D., 1963, SIAM J. Appl. Math., 11, 431

Martin D. C. et al., 2005, ApJ, 619, L1

Martin D. C. et al., 2007, ApJS, 173, 415

Meurer G. R., Heckman T. M., Calzetti D., 1999, ApJ, 521, 64

Mobasher B. et al., 2009, ApJ, 690, 1074

Morrissey P. et al., 2007, ApJS, 173, 682

Noeske K. G. et al., 2007a, ApJ, 660, L43

Noeske K. G. et al., 2007b, ApJ, 660, L47

Press W. H., Teukolsky S. A., Vetterling W. T., Flannery B. P., 2002, Numerical Recipes in C++: The Art of Scientific Computing. Cambridge Univ. Press, Cambridge

Salim S. et al., 2007, ApJS, 173, 267

Salim S., Lee J. C., 2012, ApJ, 758, 134

Salpeter E. E., 1955, ApJ, 121, 161

Sanders D. B., Mirabel I. F., 1996, ARA&A, 34, 749

Sargent M. T., Bthermin M., Daddi E., Elbaz D., 2012, ApJ, 747, L31

Scannapieco E., Silk J., Bouwens R., 2005, ApJ, 635, L13

Schechter P., 1976, ApJ, 203, 297

Schiminovich D. et al., 2005, ApJ, 619, L47

Schmidt M., 1968, ApJ, 151, 393

Seibert M. et al., 2005, ApJ, 619, L55

Treyer M. et al., 2005, ApJ, 619, L19

Voronoi G., 1908, J. Reine Angew. Math, 134, 198

Wyder T. K. et al., 2005, ApJ, 619, L15

APPENDIX A: CALCULATING LUMINOSITIES AND SFRs

A1 Galaxy luminosities

We used the *kcorrect v4.1.4* library (Blanton & Roweis 2007) to measure *k*-corrections for each band and each galaxy. The *kcorrect* library uses non-negative matrix factorization to fit the best combination of an eigenset of four spectral energy distributions (SEDs) with positive definite coefficients that matches the observed SED and redshift of a galaxy. The observed SEDs of WiggleZ galaxies were constructed from *GALEX* FUV, NUV and SDSS *ugriz* photometry. Due to the extreme blue colours of the WiggleZ galaxies, *kcorrect* sometimes fails and fits a single SED (the bluest) instead of a linear combination. We overcame this problem by using a single *k*-correction (the median) value for all the galaxies at a given redshift (and band). We only used galaxies for which *kcorrect* could successfully fit multiple components to the observed SED (giving a reduced χ^2 of order 1) to calculate the median *k*-corrections. In all bands the scatter between the individual *k*-corrections and the median values was smaller than the typical photometric uncertainties, so using medians does not affect the luminosity measurements. This is reasonable considering the small colour range of WiggleZ galaxies. The median *k*-corrections for the FUV, NUV, *g*, *r* and *i* bands are plotted in Fig. A1. Note that we calculate the FUV luminosity from the NUV apparent magnitude, as many of the galaxies were not detected in the FUV band.

A2 Star formation rates

We calculated SFRs using a Salpeter (1955) IMF and the corresponding SFR estimator of Kennicutt (1998):

$$\mathrm{SFR}\,(\mathrm{M_\odot\,yr^{-1}}) = 1.4 \times 10^{-28} \times L,$$

where *L* is the galaxy luminosity in erg s^{-1} Hz^{-1}. We measured the luminosity from 1500 to 2500 Å as this minimizes contamina-
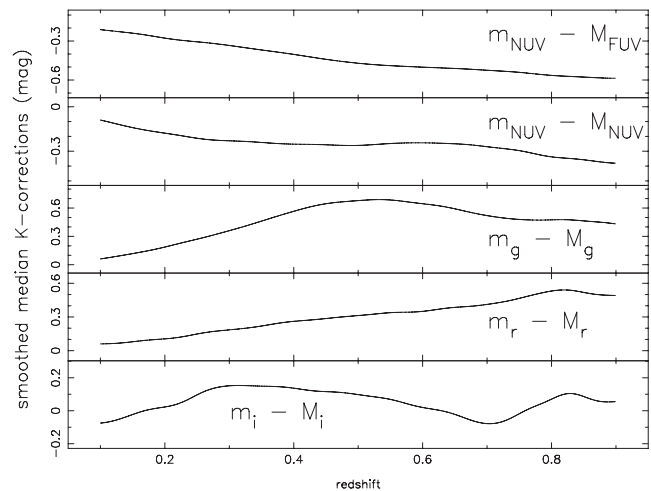
Figure A1. *k*-corrections applied to the WiggleZ galaxies as a function of redshift. The value is the median for all galaxies at each redshift for which reliable, individual *k*-corrections were provided by the *kcorrect v4.1.4* code.
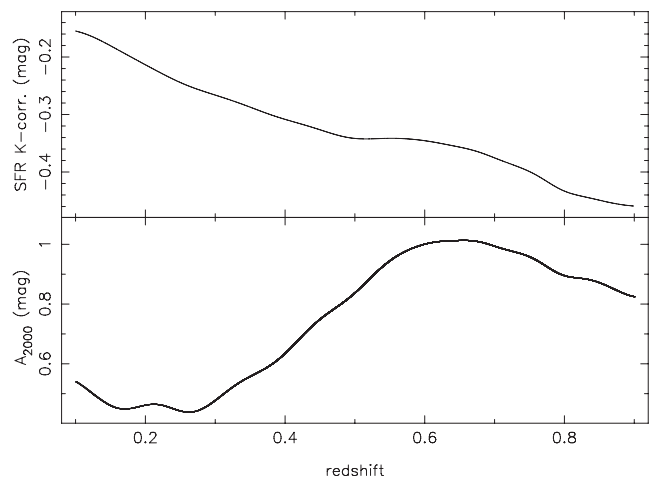
Figure A2. The Gaussian smoothed median *k*-correction (top) and corrections for internal dust (bottom) as a function of redshift. We use these to derive SFRs from the apparent NUV magnitudes.

tion of UV emission from other more long-lived stars, and avoids the Lyman α feature (Kennicutt 1998). We calculated the luminosities using median *k*-corrections (calculated as above and plotted in the top panel of Fig. A2) from the apparent NUV magnitudes to a rest-wavelength band defined by a top-hat filter from 1500 to 2500 Å.

We used the β–IRX correlation (Calzetti et al. 1994, 2000; Meurer et al. 1999) between the UV slope (β) of a galaxy spectrum and the excess infrared flux due to dust (IRX) to predict the UV dust attenuation (e.g. Seibert et al. 2005). The relation depends on galaxy type and luminosity (Bell 2002; Cortese et al. 2008), but our galaxy colours cluster around NUV $- r \sim 1$ (see fig. 5 of Drinkwater et al. 2010) so we adopt a single β–IRX relation calibration, for starburst galaxies (Seibert et al. 2005). (The reddest WiggleZ galaxies are more like Im or Sc galaxies, but the relation for quiescently star-forming spiral galaxies (Salim et al. 2007) changes the dust correction by at most 0.1 mag which is small compared to the scatter in these relations.) The WiggleZ galaxies have a small range of luminosity at each redshift, so we can use a calibration which is only a function of redshift. The Seibert et al. (2005) calibration gives the

dust correction for the FUV band. To obtain the dust correction at 2000 Å, we scale the correction by 0.857 (calculated from the Large Magellanic Cloud extinction curve in equation 4 of Calzetti et al. 2000). The 2000 Å dust correction is therefore

$$A_{2000} \text{ (mag)} = 0.857 \times (1.74\beta + 3.79),$$

where $\beta = 2.286(\text{FUV} - \text{NUV}) - 2.096$ (also in accordance with Seibert et al. 2005). The median dust correction of our sample is plotted as a function of redshift in the bottom panel of Fig. A2.

APPENDIX B: REFERENCE GALAXY SAMPLES

We constructed optical- ($R < 22.5$) and NUV- ($\text{NUV} < 22.8$) limited galaxy samples to compare with the WiggleZ selection using the AEGIS region of the DEEP2 optical redshift survey (Davis et al. 2003, 2007). We chose this region because it also has deep *GALEX* UV imaging (Davis et al. 2007) for a common area of ∼0.75 square degrees, slightly smaller than a single *GALEX* field. The AEGIS region also has more complete spectroscopic data than other DEEP2 regions: the redshift completeness ranges from 60 per cent (at $R = 21.5$) to 40 per cent ($R = 22.5$). The DEEP2 photometry is complete to $B < 24.5$, $R < 24.2$ and $I < 23.5$ and accurate to ∼0.02 mag (at 18 mag) (Coil et al. 2004).[5] The astrometry is accurate to 0.5 arcsec (Davis et al. 2003, 2007).

The *GALEX* UV observations of the AEGIS region consisted of 90 exposures, each the equivalent of a normal MIS exposure (as used for the WiggleZ survey). The *GALEX* point spread function is relatively large, leading to possible confusion at these faint magnitudes, so the UV photometry was based on positions from deep optical *r*-band imaging from the CFHTLS (Martin et al. 2007). The resulting catalogue has FUV, NUV, u^*, g', r', i' and z' photometry complete to 25, 25, 27, 28.3, 27.5, 27 and 26.4 mag, respectively, with astrometry accurate to 0.2 arcsec (Davis et al. 2007; Martin et al. 2007). This *GALEX*/CFHTLS catalogue does not include any CFHTLS optical sources where a deep *GALEX* source was not detected. We matched the DEEP2 and *GALEX*/CFHTLS catalogues with a matching radius of 1 arcsec after applying a magnitude limit of $r < 23$ to the *GALEX*/CFHTLS catalogue to reduce confusion by fainter sources. This process matched 97 per cent of the *GALEX*/CFHTLS sources to DEEP2 sources. We calculated SFRs using the DEEP2 *B* magnitudes and/or the *GALEX* NUV magnitudes as available. The two estimates were consistent when both measurements were available.

The optical reference sample was constructed by taking all the DEEP2 sources brighter than $R = 22.5$ for which a redshift was measured, with the corresponding *GALEX*/CFHTLS photometry if available. No UV photometry was used in the definition of this sample. The spectroscopic completeness weights for this sample were calculated as a function of their R magnitude.

The UV reference sample was constructed from the combined DEEP2 and *GALEX*/CFHTLS catalogue by selecting *GALEX* sources brighter than $\text{NUV} = 22.8$ and requiring that the redshift was measured in DEEP2. There is an implied optical limit ($R < 24.2$) in this process, but a negligible number of galaxies was excluded by this limit. The weighting for spectroscopic completeness was again calculated according to R magnitude.

The AEGIS field is not part of the WiggleZ survey, but we simulated 90 independent realizations of a *GALEX* MIS observation of the same set of objects as follows. First, we matched each *GALEX* MIS observation to the combined DEEP2 and *GALEX*/CFHTLS catalogue with nearest-neighbour matching in a radius of 5.5 arcsec (determined as above and using the CFHTLS astrometry for consistency). We then converted the CFHTLS $g'r'i$ photometry to SDSS gri using colour equations from Gwynn (private communication) so that we could apply the WiggleZ target selection criteria to each sample.

APPENDIX C: SELECTION FUNCTION

C1 UV and optical images

The WiggleZ survey extends fainter than the 100 per cent completeness limits of its two main selection bands (NUV and optical *r*; see Table 2). The selection function therefore includes terms for the completeness (the probability that a galaxy is detected) of these two input catalogues as a function of the apparent magnitude.

We measured both the NUV and *r* completeness functions using the same method. We fitted curves of the following form to the number counts in each band:

$$N(m) = 10^{\alpha m + \beta} 0.5(1 + \text{erf}((\gamma - m)/\theta)),$$

where the error function term describes the deviation from power-law counts as the sample becomes less complete at faint magnitudes. Using these fits, the completeness of a magnitude m galaxy is

$$C(m) = 0.5(1 + \text{erf}((\gamma - m)/\theta)).$$

We fitted the curves using the Levenberg–Marquardt method (Levenberg 1944; Marquardt 1963) and the implementation in Press et al. (2002). To avoid singularities in phase space when fitting, we seed the Levenberg–Marquardt method with the result of a χ^2 minimization. We used the covariance matrices provided by this method to obtain the uncertainties in the fitted parameters and $C(m)$. We show an example of this curve-fitting approach and the corresponding completeness in Fig. C1.

We measured the NUV completeness in each *GALEX* tile separately as the exposures varied significantly from tile to tile. For the optical (SDSS *r*-band) catalogues, there was no evidence of any significant variation in completeness across any of the survey rectangles, so we fitted a single completeness function to each survey rectangle.

C2 Spectroscopic completeness

We define the spectroscopic completeness as the probability of a target being observed and the observation resulting in a redshift. For the LF calculation, it is sufficient to calculate the average of this function over each *GALEX* tile. This is in contrast to our clustering measurements where all the spatial information must be measured (e.g. Blake et al. 2009).

During the survey we prioritized the targets for spectroscopic observation on the basis of *r*-band magnitude (see Table 2). We therefore measured the spectroscopic completeness for each priority band separately. We used binomial statistics to estimate the uncertainty in these completeness values.

---

[5] Brown et al. (2007) found that there is a systematic uncertainty in the DEEP2 photometry, with DEEP2 systematically underestimating the *B*, *R* and *I*photometry by ∼0.15 mag. As we only use the DEEP2 data set for an internal comparison to itself, this is not a significant problem.
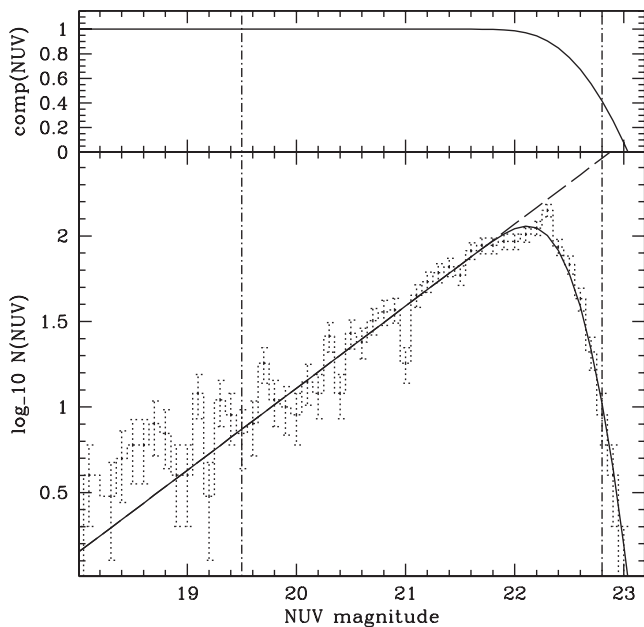
Figure C1. The completeness function calculated for an example *GALEX* NUV observation. Lower panel: the measured NUV number counts (dotted line) compared to the fitted model (solid line). The underlying power law from the model fit is shown by the dashed line. The vertical lines show the bright limit of the fit (to avoid contamination of the power-law slope by stars) and the faint limit of the main WiggleZ survey. Upper panel: the resulting completeness function for this observation given by the difference between the solid and dashed lines in the lower panel.

C3 Modelling FUV aperture magnitudes

The FUV − NUV colour selection – unlike the other colour selection terms in Table 2 – does not impose a direct constraint on a galaxy's observable redshift range. This is partly because this criterion allows a galaxy to satisfy the FUV − NUV colour selection in two different ways (FUV − NUV ≥ 1 or undetected in the FUV). The other contributing factor is that aperture photometry was used for the FUV magnitudes. We include the FUV − NUV colour selection in the selection function by treating it as an additional completeness term, $C_{\mathrm{FUVap\,corr}}$. In this section, we present a model of the FUV measurements and test it against our *GALEX* data. We then use it to calculate the FUV − NUV completeness term.

The WiggleZ FUV measurements were calculated in 6 arcsec apertures centred on the NUV detections (Drinkwater et al. 2010). This had the disadvantage that many of the fainter FUV measurements are dominated by random noise and background subtraction artefacts. We modelled the FUV aperture fluxes as the sum of a source flux and a local background flux. We measured the distribution of background fluxes in each *GALEX* tile using the point sources (radius ≤ 5 arcsec) detected at S/N ≥ 3 in the NUV. We measured the FUV background flux for each point source from the difference of two apertures significantly larger than the source (17.3 and 12.8 arcsec). Note that we apply the aperture corrections in Morrissey et al. (2007) when calculating background fluxes.

We tested this model by predicting the distribution of FUV aperture magnitudes as shown in Fig. C2. As in Appendix C1, we assumed a power-law underlying source distribution and fitted the
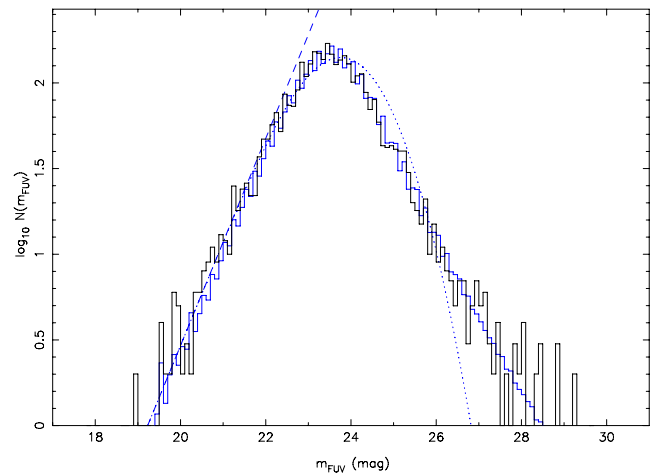
Figure C2. The actual and predicted aperture FUV magnitude distributions for a random *GALEX* tile are plotted in the bottom panel as solid black and blue lines (0.1 mag bins). The predicted distribution is a good match to the actual FUV aperture magnitude distribution. The process used to predict the aperture FUV distribution is traced by the blue dashed (initial source flux distribution), blue dotted (detected source fluxes) and blue solid lines (aperture correction applied and scattered by background fluxes). The contributions of the background fluxes to the observed aperture magnitudes are plotted in the top panel. The solid line in the top panel is plotted as a reference line. Above this line, the background fluxes dominate the aperture FUV magnitudes.

standard distribution function,

$$N(m) = 10^{\alpha m + \beta}0.5(1 + \mathrm{erf}((\gamma - m)/\theta)),$$

to the aperture FUV distribution for $m_{\mathrm{FUV}} \leq 25.35$. This is sufficiently bright that the source fluxes dominate the aperture FUV magnitudes. We then added a random background contribution to the galaxies at each magnitude using the background flux distribution. The predicted counts from this model agree much better with the data than the normal completeness function (Fig. C2). Note that no fitting was carried out to match the faint end of the aperture FUV distribution. We confirmed that the model predictions for all *GALEX* tiles used in our analysis matched the measured aperture FUV distributions.

We incorporated this model of the FUV aperture magnitudes into the selection function as follows. We predicted the apparent FUV and NUV model magnitudes of a galaxy at each redshift and applied the aperture correction to obtain the source flux contribution to the FUV aperture magnitude. We then used the background flux distribution (for the *GALEX* tile) to determine the probability that the sum of the source flux and background would give FUV − NUV ≥ 1, which we denote by C_{UVcol}. Finally, we combine this with the tile's detection rate [this is $C(m)$ for the FUV band], C_{FUV}, to calculate $C_{\mathrm{FUVap\,corr}}$ for this galaxy as a function of redshift,

$$C_{\mathrm{FUVap\,corr}} = (C_{\mathrm{FUV}} \times C_{\mathrm{UVcol}}) + (1 - C_{\mathrm{FUV}}).$$

The first term is the probability that the source is detected and satisfies FUV − NUV > 1 and the second term is the probability that the FUV is not detected. The main effect of this $C_{\mathrm{FUVap\,corr}}$ 'completeness' is to add an effective low-redshift limit to the observable volume. For luminous galaxies ($M_{\mathrm{NUV}} \leq -20.5$) the first term dominates because the galaxy is detected in both FUV and NUV and produces accurate FUV − NUV colours at $z < 0.6$. The FUV − NUV > 1 colour term then functions as intended to impose a redshift limit of $z < 0.6$. As the galaxies become less luminous,

the second term starts to dominate as the FUV detection fails, so the cutoff redshift moves to lower redshifts.

APPENDIX D: DETAILS OF LF RESULTS

D1 LF diagnostics

The $1/V_{MAX}$ estimator assumes that each galaxy is a single realization of a Poisson process within the galaxy's maximum observable volume. This is not valid in the presence of galaxy evolution and/or clustering. We tested this assumption by calculating the mean value of the statistic V_e/V_{MAX} at each redshift, where V_e is the volume interior to a galaxy's redshift and V_{MAX} is the maximum observable volume discussed earlier; if the $1/V_{MAX}$ assumption holds, the sample mean of V_e/V_{MAX} is 0.5 and the standard deviation is $1/\sqrt{12\,N}$ (Avni & Bahcall 1980). We calculated the mean values and uncertainties of V/V_{MAX} for the samples in each $\Delta z = 0.05$ redshift interval. The uncertainties were dominated by systematic uncertainties in the volumes (typically 5 per cent) as the large sample size gave very small statistical uncertainties. In each bin measured, the mean V_e/V_{MAX} was not significantly different from 0.5, although the differences became significant if the redshift bins were any larger. Therefore, we can reliably apply the $1/V_{MAX}$ estimator to our sample in the redshift bins we have chosen.

We also tested the V_{MAX} calculations by calculating the LFs separately in the three different survey regions and comparing the results. For this purpose, we integrated the LFs over the whole $0.1 < z < 0.9$ redshift range. The result is not a true LF as the redshift range varies with luminosity, but it does serve as a measure of the total counts at each luminosity in each field. The resulting functions, shown in Fig. D1, show no systematic differences between fields.
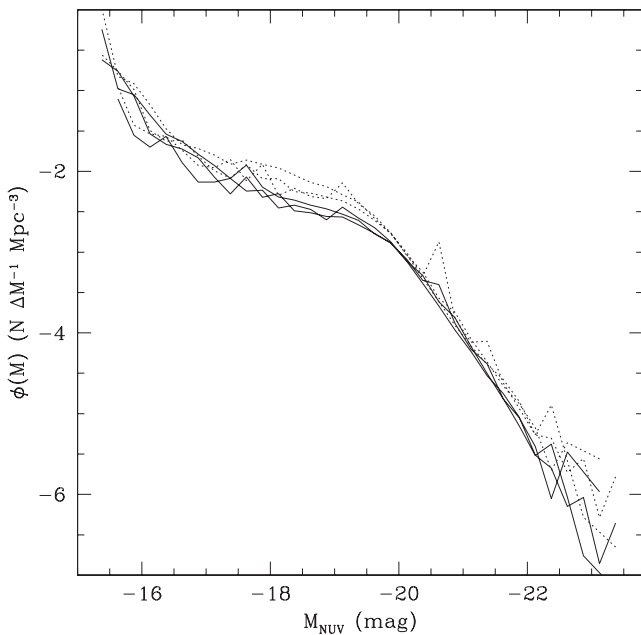
Figure D1. Comparison of the integrated NUV LFs in the three survey regions. For each of the survey regions, the LF (Fig. 5) is integrated over the full redshift range ($0.1 < z < 0.9$) and plotted as a single solid line. In each case, a second dotted curve shows the LF corrected for the LRR cuts. The uncertainties are not plotted for clarity, but these are typically ~0.2 dex. Note that these are not true LFs – each luminosity bin covers a different redshift range – but they serve to demonstrate the absence of any systematic differences between the survey fields.
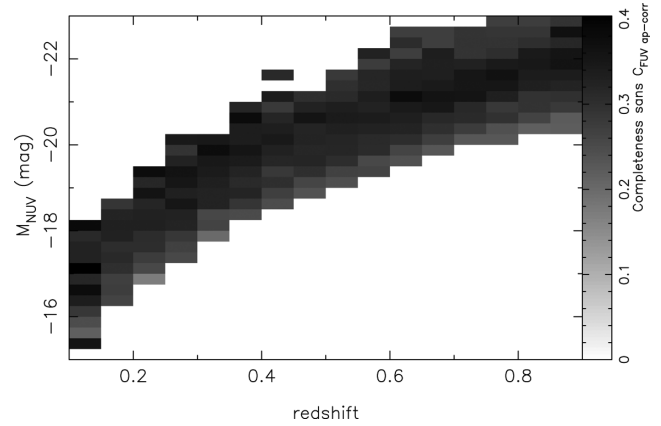
Figure D2. Completeness correction applied to the LFs. At each point in luminosity–redshift space, the ratio of the raw LF values to the final corrected LF value is plotted. These ratios are equivalent to the typical completeness applied, the C_{NUV}, C_r and C_{spec} terms in the selection function.

We also show in Fig. D1 the integrated LFs after correction for the LRR cuts (as dotted lines). These also demonstrate no significant difference between fields, showing that our calculation of the LRR correction is consistent across the survey. We repeated this analysis for the *r*-band LFs. These are not plotted, but they show a similarly close agreement between the three survey regions (with and without the LRR correction), again indicating that there are no systematic errors between the fields. Fig. D1 also demonstrates that our survey region is sufficiently large to minimize the effects of cosmic variance on our results.

To illustrate the importance of the completeness corrections on the LF, we calculated a 'raw' 2D NUV LF, with no correction for the survey completeness. We plot the ratio of the raw 2D LF to the final corrected 2D NUV LF in Fig. D2. The ratio is equivalent to the typical completeness of the WiggleZ selection function as a function of redshift and M_{NUV}. The selection function mean is 0.31 and varies from 0.17 to 0.404. The typical values of the C_{NUV}, C_r and C_{spec} terms of the selection function are consistent with these values.
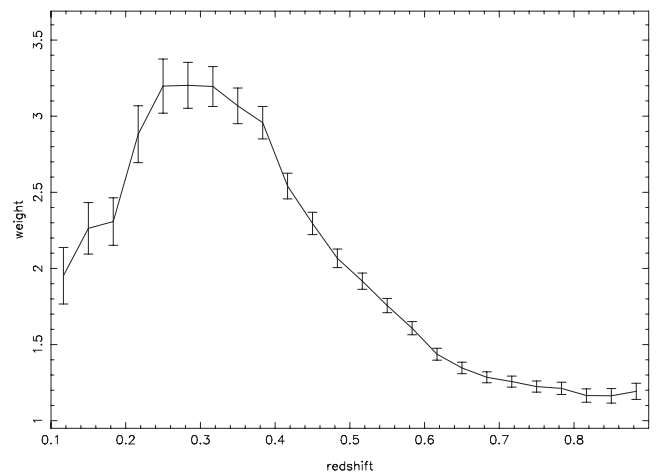
Figure D3. The correction factor for galaxies removed from the WiggleZ sample by the LRR criteria. This was calculated by retrospectively applying the LRR criteria to WiggleZ survey observations obtained prior to 2007 April (when the LRR cuts were first adopted). The 1σ uncertainties are shown, calculated assuming binomial statistics.
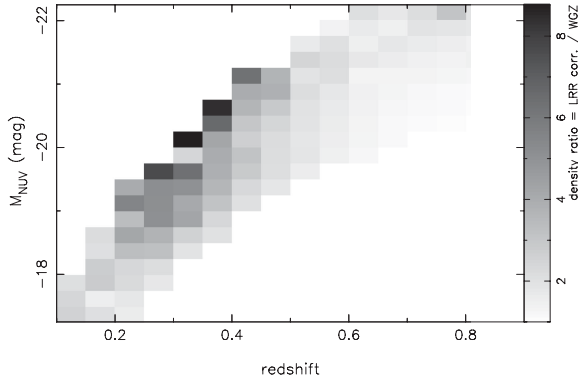
Figure D4. The correction for the LRR cuts applied to the NUV LF. Each cell of the plot shows the ratio of the LRR-corrected to the uncorrected comoving number density of galaxies. This ratio is equivalent to the mean correction that is applied to a given grid element, to obtain the LRR-corrected 2D NUV LF.

D2 Correcting the LF for the LRR cuts

We estimate a correction for the galaxies removed by the LRR criteria by making two modifications to the approach described in Section 4.

The first modification is to add an additional completeness term to the V_{MAX} calculation which describes the probability that a galaxy was removed by the LRR cuts. We calculated this completeness by retrospectively applying the LRR cuts to WiggleZ data obtained before 2007 April (when the LRR cuts were introduced) to calculate the fraction of galaxies rejected as a function of redshift and r magnitude. The second modification was to not apply the LRR colour limits when determining a galaxy's observable redshift range. If we did not re-measure the observable redshift range, we would be artificially truncating the LRR-corrected V_{MAX} values. The resulting correction factor (averaged over r magnitude) is shown in Fig. D3.

In calculating the correction, we are assuming that the selection of the galaxies previously rejected by the LLR cuts can be simulated as a function of just z and r. To test this assumption, we
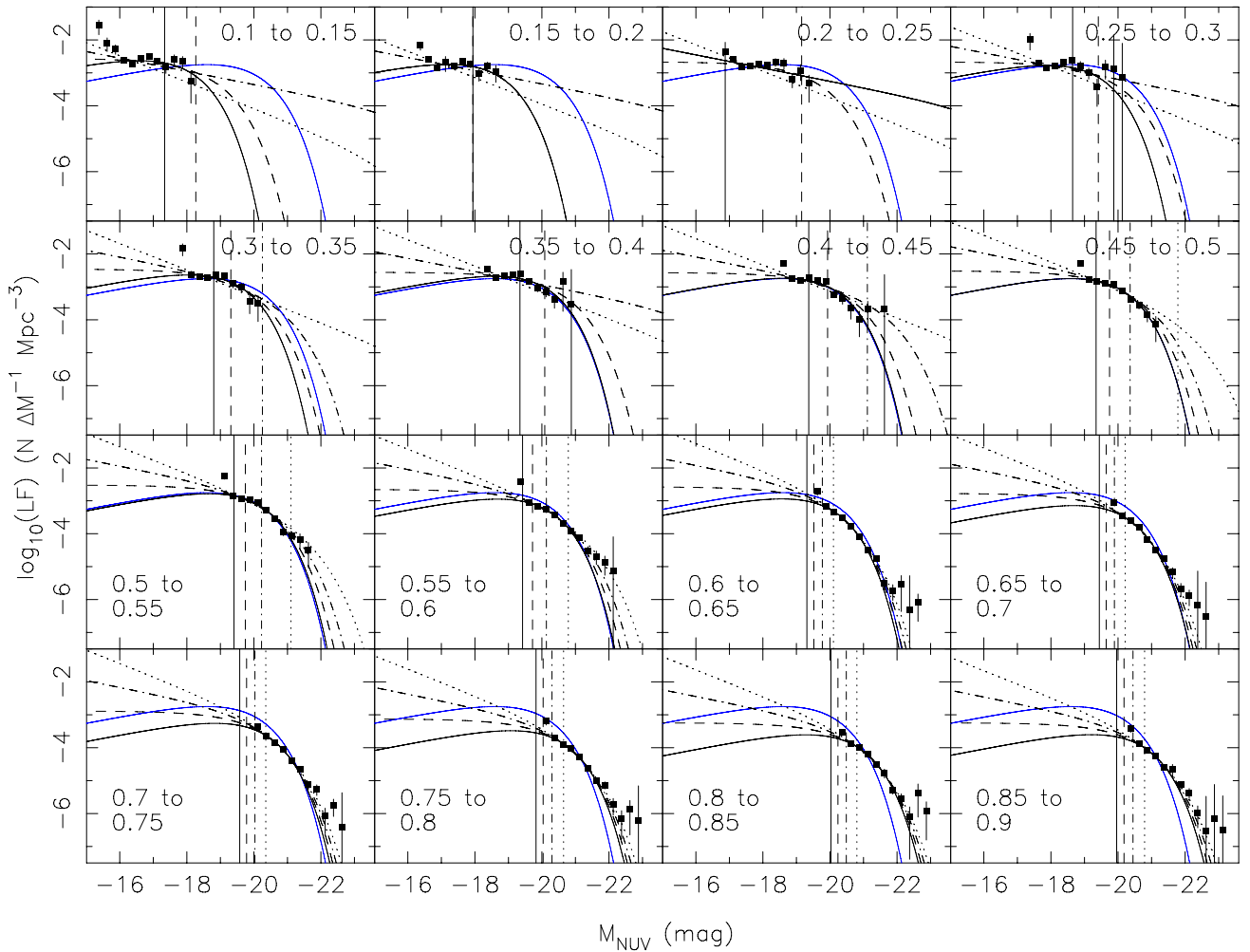
Figure D5. The LRR-corrected, NUV LFs of WiggleZ galaxies at 16 independent redshifts. The solid, dashed, dot–dashed and dotted lines correspond to Schechter function fits using fixed faint-end slopes of $\alpha = -0.5, -1.0, -1.5$ and -2. The vertical lines indicate the fitted $M*$ parameters for these fits using the same line styles. The $\alpha = -1$, $0.4 < z < 0.45$ fit is overplotted in blue as a visual reference.

independently estimated the correction using the DEEP2 reference galaxy samples described in Appendix B. We then compared the mean redshift distributions (incorporating the DEEP2 spectroscopic weights) of the non-LRR WiggleZ samples and WiggleZ samples to obtain a predicted correction factor. The predicted corrections were consistent with the observed values in Fig. D3 (assuming binomial statistics). We show the effect of this correction on the LFs in Fig. D4, which plots the ratio of the corrected to the uncorrected LFs as a function of redshift and luminosity.

D3 Additional LFs

We present the NUV LF corrected for the LRR cuts, and the *r*-band LFs without and with corrections for the LRR cuts in Figs D5, D6 and D7, respectively.

D4 Numerical values

We present the numerical values for the LFs in Tables D1–D4, and the values of analytic fits to them in Tables D5–D8.
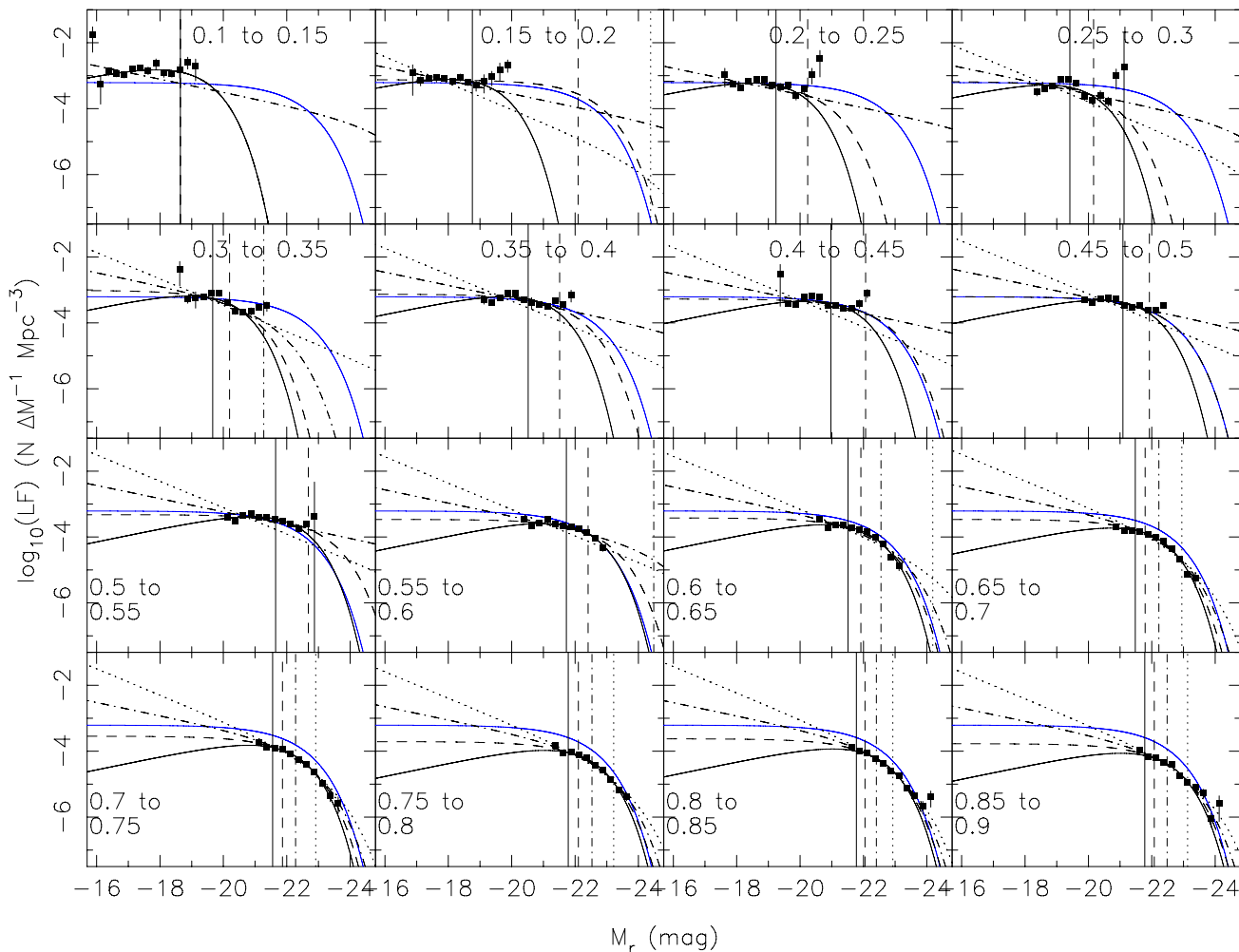
Figure D6. The *r* LFs of WiggleZ galaxies at 16 independent redshifts. The solid, dashed, dot–dashed and dotted lines correspond to Schechter function fits using fixed faint-end slopes of $\alpha = -0.5, -1.0, -1.5$ and -2. The vertical lines indicate the fitted M^* parameters for these fits using the same line styles. The $\alpha = -1, 0.4 < z < 0.45$ fit is overplotted in blue as a visual reference.
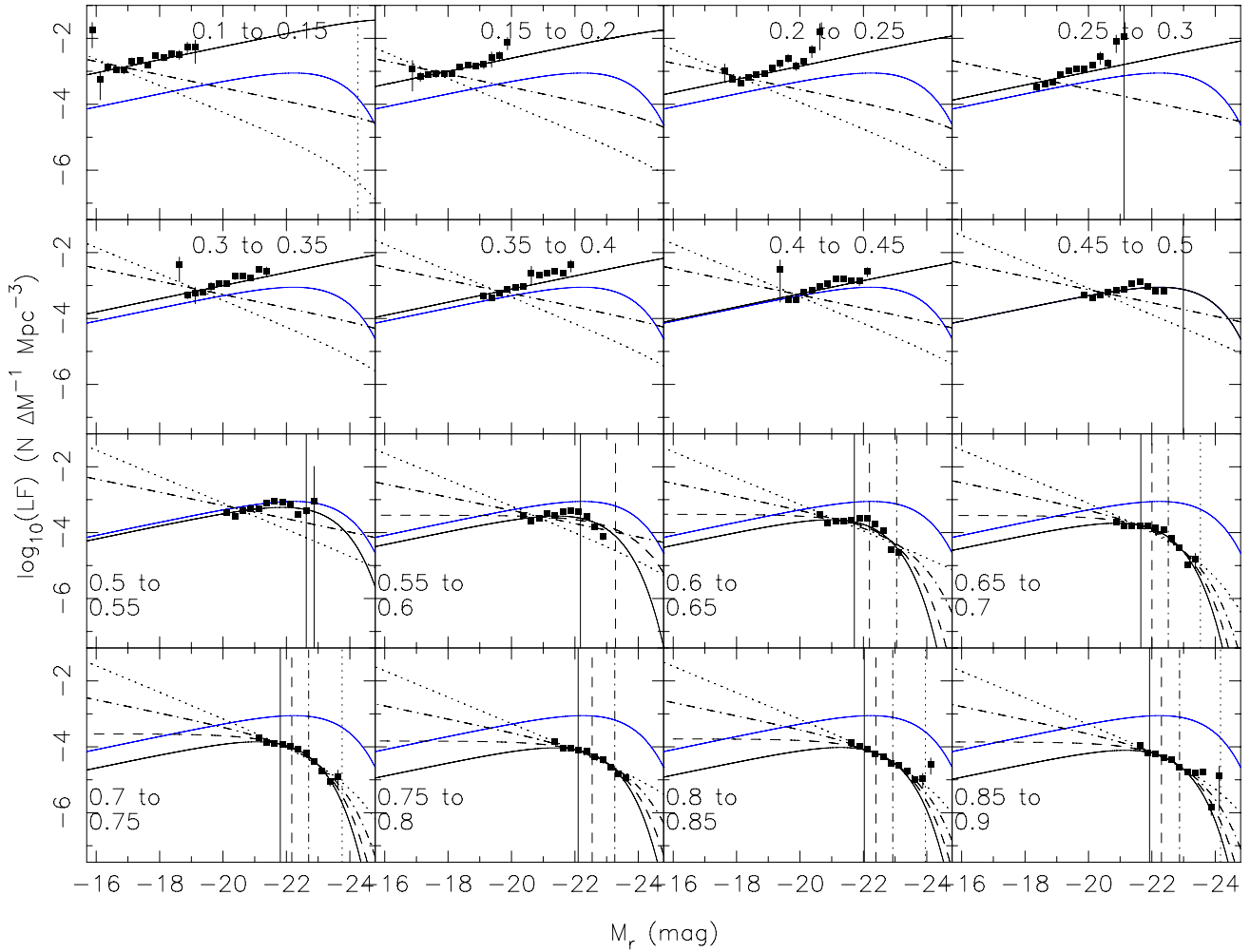
Figure D7. The LRR-corrected, *r* LFs of WiggleZ galaxies at 16 independent redshifts. The solid, dashed, dot–dashed and dotted lines correspond to Schechter function fits using fixed faint-end slopes of $\alpha = -0.5$, -1.0, -1.5 and -2. The vertical lines indicate the fitted M^* parameters for these fits using the same line styles. The $\alpha = -0.5$, $0.4 < z < 0.45$ fit is overplotted in blue as a visual reference.

Table D1. Numerical values (and uncertainties) for the NUV LFs of WiggleZ galaxies.

| z: M_{NUV}	0.125	0.175	0.225	0.275	0.325	0.375	0.425	0.475
−15.5	$-1.77^{+0.16}_{-0.27}$							
−15.75	$-2.17^{+0.18}_{-0.30}$							
−16	$-2.41^{+0.14}_{-0.22}$							
−16.25	$-2.72^{+0.06}_{-0.07}$							
−16.5	$-2.78^{+0.07}_{-0.09}$	$-2.32^{+0.11}_{-0.15}$						
−16.75	$-2.71^{+0.09}_{-0.11}$	$-2.75^{+0.05}_{-0.06}$						
−17	$-2.66^{+0.10}_{-0.12}$	$-2.97^{+0.09}_{-0.11}$	$-2.38^{+0.31}_{-2.38}$					
−17.25	$-2.95^{+0.10}_{-0.13}$	$-2.96^{+0.09}_{-0.11}$	$-2.73^{+0.07}_{-0.08}$					
−17.5	$-3.24^{+0.12}_{-0.16}$	$-3.11^{+0.05}_{-0.06}$	$-3.03^{+0.04}_{-0.04}$	$-2.38^{+0.16}_{-0.24}$				
−17.75	$-2.96^{+0.12}_{-0.16}$	$-2.82^{+0.13}_{-0.18}$	$-3.03^{+0.04}_{-0.04}$	$-2.86^{+0.05}_{-0.05}$				
−18	$-2.96^{+0.15}_{-0.23}$	$-3.18^{+0.08}_{-0.10}$	$-3.10^{+0.06}_{-0.07}$	$-3.10^{+0.05}_{-0.06}$	$-1.99^{+0.17}_{-0.29}$			
−18.25	$-3.22^{+0.31}_{-3.22}$	$-3.47^{+0.12}_{-0.17}$	$-3.12^{+0.11}_{-0.15}$	$-3.13^{+0.04}_{-0.04}$	$-2.93^{+0.04}_{-0.04}$			
−18.5		$-3.12^{+0.17}_{-0.28}$	$-3.19^{+0.08}_{-0.11}$	$-3.20^{+0.05}_{-0.05}$	$-2.97^{+0.12}_{-0.17}$	$-2.70^{+0.04}_{-0.05}$		
−18.75		$-3.30^{+0.24}_{-0.59}$	$-3.32^{+0.11}_{-0.14}$	$-3.20^{+0.07}_{-0.08}$	$-3.14^{+0.03}_{-0.04}$	$-3.03^{+0.03}_{-0.03}$	$-2.58^{+0.05}_{-0.06}$	
−19			$-3.72^{+0.15}_{-0.24}$	$-3.50^{+0.11}_{-0.15}$	$-3.26^{+0.04}_{-0.04}$	$-3.05^{+0.03}_{-0.03}$	$-3.02^{+0.02}_{-0.02}$	$-2.48^{+0.05}_{-0.05}$
−19.25			$-3.67^{+0.18}_{-0.30}$	$-3.69^{+0.05}_{-0.12}$	$-3.26^{+0.05}_{-0.06}$	$-3.13^{+0.03}_{-0.03}$	$-3.10^{+0.03}_{-0.04}$	$-2.99^{+0.02}_{-0.03}$
−19.5			$-3.92^{+0.26}_{-0.75}$	$-4.15^{+0.17}_{-0.29}$	$-3.60^{+0.08}_{-0.10}$	$-3.18^{+0.03}_{-0.04}$	$-3.09^{+0.10}_{-0.14}$	$-3.10^{+0.02}_{-0.02}$
−19.75				$-3.70^{+0.18}_{-0.30}$	$-3.81^{+0.09}_{-0.11}$	$-3.41^{+0.06}_{-0.07}$	$-3.27^{+0.03}_{-0.03}$	$-3.21^{+0.02}_{-0.02}$
−20				$-3.74^{+1.04}_{-3.74}$	$-3.81^{+0.29}_{-1.15}$	$-3.64^{+0.09}_{-0.11}$	$-3.33^{+0.05}_{-0.05}$	$-3.27^{+0.02}_{-0.03}$
−20.25				$-4.24^{+1.04}_{-4.24}$	$-4.44^{+0.24}_{-0.59}$	$-3.77^{+0.12}_{-0.17}$	$-3.65^{+0.11}_{-0.15}$	$-3.46^{+0.04}_{-0.04}$
−20.5						$-4.21^{+0.15}_{-0.24}$	$-3.84^{+0.13}_{-0.19}$	$-3.77^{+0.06}_{-0.08}$
−20.75						$-3.76^{+0.27}_{-0.81}$	$-4.21^{+0.19}_{-0.35}$	$-4.03^{+0.08}_{-0.10}$
−21						$-4.39^{+1.04}_{-4.39}$	$-4.58^{+0.24}_{-0.57}$	$-4.43^{+0.14}_{-0.22}$
−21.25							$-4.47^{+0.23}_{-0.54}$	$-4.70^{+0.23}_{-0.54}$
−21.75							$-4.20^{+1.04}_{-4.20}$	

z: M_{NUV}	0.525	0.575	0.625	0.675	0.725	0.775	0.825	0.875
−19.25	$-2.44^{+0.06}_{-0.07}$							
−19.5	$-3.02^{+0.02}_{-0.02}$	$-2.59^{+0.09}_{-0.11}$						
−19.75	$-3.14^{+0.02}_{-0.02}$	$-3.19^{+0.02}_{-0.02}$	$-2.83^{+0.07}_{-0.08}$					
−20	$-3.24^{+0.02}_{-0.02}$	$-3.33^{+0.02}_{-0.02}$	$-3.26^{+0.02}_{-0.02}$	$-3.13^{+0.05}_{-0.06}$				
−20.25	$-3.32^{+0.03}_{-0.03}$	$-3.44^{+0.03}_{-0.03}$	$-3.46^{+0.02}_{-0.02}$	$-3.53^{+0.02}_{-0.02}$	$-3.40^{+0.04}_{-0.04}$	$-3.24^{+0.09}_{-0.11}$		
−20.5	$-3.56^{+0.04}_{-0.04}$	$-3.63^{+0.03}_{-0.03}$	$-3.64^{+0.02}_{-0.02}$	$-3.68^{+0.02}_{-0.03}$	$-3.70^{+0.02}_{-0.03}$	$-3.73^{+0.02}_{-0.02}$	$-3.54^{+0.04}_{-0.05}$	$-3.42^{+0.10}_{-0.13}$
−20.75	$-3.83^{+0.06}_{-0.07}$	$-3.92^{+0.04}_{-0.04}$	$-3.90^{+0.02}_{-0.02}$	$-3.88^{+0.03}_{-0.03}$	$-3.91^{+0.02}_{-0.03}$	$-3.95^{+0.02}_{-0.02}$	$-3.91^{+0.03}_{-0.03}$	$-3.90^{+0.03}_{-0.03}$
−21	$-4.28^{+0.09}_{-0.11}$	$-4.16^{+0.05}_{-0.05}$	$-4.25^{+0.03}_{-0.03}$	$-4.27^{+0.03}_{-0.04}$	$-4.13^{+0.03}_{-0.03}$	$-4.09^{+0.05}_{-0.06}$	$-4.04^{+0.03}_{-0.03}$	$-4.13^{+0.03}_{-0.03}$
−21.25	$-4.34^{+0.13}_{-0.19}$	$-4.43^{+0.07}_{-0.08}$	$-4.63^{+0.06}_{-0.07}$	$-4.62^{+0.04}_{-0.05}$	$-4.53^{+0.04}_{-0.04}$	$-4.38^{+0.03}_{-0.04}$	$-4.29^{+0.04}_{-0.04}$	$-4.31^{+0.03}_{-0.04}$
−21.5	$-4.56^{+0.16}_{-0.27}$	$-4.86^{+0.12}_{-0.17}$	$-4.98^{+0.07}_{-0.08}$	$-4.94^{+0.07}_{-0.08}$	$-4.81^{+0.07}_{-0.08}$	$-4.76^{+0.04}_{-0.05}$	$-4.64^{+0.04}_{-0.04}$	$-4.69^{+0.04}_{-0.05}$
−21.75	$-4.73^{+0.23}_{-0.54}$	$-4.99^{+0.15}_{-0.24}$	$-5.67^{+0.17}_{-0.30}$	$-5.42^{+0.10}_{-0.09}$	$-5.35^{+0.08}_{-0.14}$	$-5.19^{+0.06}_{-0.08}$	$-4.91^{+0.14}_{-0.20}$	$-4.94^{+0.07}_{-0.09}$
−22		$-5.02^{+0.20}_{-0.38}$	$-5.96^{+0.18}_{-0.32}$	$-5.83^{+0.18}_{-0.33}$	$-5.54^{+0.11}_{-0.15}$	$-5.41^{+0.08}_{-0.10}$	$-5.50^{+0.09}_{-0.11}$	$-5.38^{+0.07}_{-0.08}$
−22.25		$-5.52^{+1.04}_{-5.52}$	$-5.86^{+0.26}_{-0.73}$	$-6.13^{+0.18}_{-0.30}$	$-6.41^{+0.23}_{-0.54}$	$-6.09^{+0.16}_{-0.26}$	$-5.79^{+0.12}_{-0.17}$	$-5.66^{+0.10}_{-0.12}$
−22.5			$-6.61^{+1.04}_{-6.61}$	$-6.26^{+1.04}_{-6.26}$	$-6.11^{+0.18}_{-0.30}$	$-6.48^{+0.23}_{-0.54}$	$-6.46^{+0.24}_{-0.59}$	$-6.28^{+0.18}_{-0.31}$
−22.75			$-6.25^{+0.23}_{-0.54}$	$-6.64^{+1.04}_{-6.64}$	$-6.71^{+1.04}_{-6.71}$	$-6.44^{+0.23}_{-0.54}$	$-6.03^{+0.25}_{-0.63}$	$-6.85^{+1.04}_{-6.85}$
−23						$-6.72^{+1.04}_{-6.72}$	$-6.39^{+0.23}_{-0.53}$	$-6.85^{+1.04}_{-6.85}$
−23.25								$-6.77^{+1.04}_{-6.77}$

Notes. (1) Values are base 10 logarithm. (2) Luminosities and redshifts correspond to bin centres.

Table D2. Numerical values (and uncertainties) for the *r*-band LFs of WiggleZ galaxies.

z: M_r	0.125	0.175	0.225	0.275	0.325	0.375	0.425	0.475
-16	$-1.75^{+0.23}_{-0.54}$							
-16.25	$-3.25^{+0.24}_{-0.61}$							
-16.5	$-2.86^{+0.11}_{-0.14}$							
-16.75	$-2.93^{+0.08}_{-0.10}$							
-17	$-2.96^{+0.09}_{-0.11}$	$-2.92^{+0.25}_{-0.68}$						
-17.25	$-2.79^{+0.08}_{-0.10}$	$-3.15^{+0.11}_{-0.16}$						
-17.5	$-2.76^{+0.07}_{-0.09}$	$-3.09^{+0.07}_{-0.08}$						
-17.75	$-2.84^{+0.10}_{-0.13}$	$-3.07^{+0.10}_{-0.13}$	$-2.97^{+0.20}_{-0.37}$					
-18	$-2.62^{+0.13}_{-0.19}$	$-3.09^{+0.06}_{-0.07}$	$-3.24^{+0.07}_{-0.09}$					
-18.25	$-2.91^{+0.10}_{-0.13}$	$-3.17^{+0.05}_{-0.06}$	$-3.36^{+0.05}_{-0.06}$					
-18.5	$-2.93^{+0.09}_{-0.12}$	$-3.04^{+0.09}_{-0.12}$	$-3.18^{+0.05}_{-0.05}$	$-3.48^{+0.10}_{-0.13}$				
-18.75	$-2.82^{+0.16}_{-0.26}$	$-3.20^{+0.08}_{-0.10}$	$-3.13^{+0.04}_{-0.05}$	$-3.39^{+0.06}_{-0.07}$	$-2.37^{+0.23}_{-0.51}$			
-19	$-2.58^{+0.14}_{-0.22}$	$-3.30^{+0.13}_{-0.18}$	$-3.11^{+0.08}_{-0.09}$	$-3.31^{+0.05}_{-0.05}$	$-3.28^{+0.10}_{-0.12}$			
-19.25	$-2.71^{+0.22}_{-0.44}$	$-3.16^{+0.20}_{-0.36}$	$-3.29^{+0.08}_{-0.09}$	$-3.12^{+0.04}_{-0.04}$	$-3.24^{+0.18}_{-0.31}$	$-3.31^{+0.09}_{-0.12}$		
-19.5		$-3.03^{+0.17}_{-0.27}$	$-3.34^{+0.11}_{-0.14}$	$-3.11^{+0.04}_{-0.05}$	$-3.21^{+0.03}_{-0.04}$	$-3.38^{+0.06}_{-0.07}$	$-2.51^{+0.28}_{-0.99}$	
-19.75		$-2.81^{+0.19}_{-0.35}$	$-3.29^{+0.10}_{-0.13}$	$-3.22^{+0.09}_{-0.11}$	$-3.08^{+0.08}_{-0.09}$	$-3.24^{+0.03}_{-0.04}$	$-3.42^{+0.05}_{-0.06}$	
-20		$-2.67^{+0.15}_{-0.23}$	$-3.61^{+0.10}_{-0.13}$	$-3.63^{+0.09}_{-0.11}$	$-3.10^{+0.08}_{-0.11}$	$-3.10^{+0.03}_{-0.10}$	$-3.43^{+0.03}_{-0.04}$	$-3.29^{+0.06}_{-0.07}$
-20.25			$-3.41^{+0.10}_{-0.12}$	$-3.75^{+0.09}_{-0.11}$	$-3.38^{+0.07}_{-0.08}$	$-3.11^{+0.03}_{-0.03}$	$-3.22^{+0.03}_{-0.03}$	$-3.37^{+0.03}_{-0.04}$
-20.5			$-2.95^{+0.18}_{-0.30}$	$-3.60^{+0.14}_{-0.21}$	$-3.65^{+0.08}_{-0.10}$	$-3.30^{+0.04}_{-0.04}$	$-3.19^{+0.03}_{-0.03}$	$-3.29^{+0.03}_{-0.03}$
-20.75			$-2.47^{+0.24}_{-0.57}$	$-3.77^{+0.11}_{-0.15}$	$-3.68^{+0.06}_{-0.08}$	$-3.37^{+0.05}_{-0.21}$	$-3.21^{+0.05}_{-0.06}$	$-3.24^{+0.02}_{-0.03}$
-21				$-3.01^{+0.21}_{-0.41}$	$-3.65^{+0.10}_{-0.13}$	$-3.44^{+0.07}_{-0.08}$	$-3.48^{+0.04}_{-0.04}$	$-3.27^{+0.04}_{-0.04}$
-21.25				$-2.73^{+1.04}_{-2.73}$	$-3.52^{+0.07}_{-0.08}$	$-3.49^{+0.06}_{-0.07}$	$-3.48^{+0.04}_{-0.05}$	$-3.48^{+0.03}_{-0.04}$
-21.5					$-3.49^{+0.12}_{-0.17}$	$-3.32^{+0.08}_{-0.09}$	$-3.57^{+0.06}_{-0.07}$	$-3.54^{+0.03}_{-0.04}$
-21.75						$-3.43^{+0.07}_{-0.09}$	$-3.55^{+0.05}_{-0.05}$	$-3.48^{+0.03}_{-0.04}$
-22						$-3.15^{+0.14}_{-0.21}$	$-3.41^{+0.11}_{-0.14}$	$-3.61^{+0.04}_{-0.05}$
-22.25							$-3.10^{+0.11}_{-0.14}$	$-3.61^{+0.05}_{-0.05}$
-22.5								$-3.48^{+0.08}_{-0.09}$

z: M_r	0.525	0.575	0.625	0.675	0.725	0.775	0.825	0.875
-20.25	$-3.39^{+0.07}_{-0.08}$							
-20.5	$-3.51^{+0.03}_{-0.03}$	$-3.47^{+0.08}_{-0.09}$						
-20.75	$-3.33^{+0.04}_{-0.05}$	$-3.66^{+0.03}_{-0.04}$	$-3.46^{+0.06}_{-0.07}$					
-21	$-3.30^{+0.02}_{-0.02}$	$-3.57^{+0.02}_{-0.02}$	$-3.72^{+0.03}_{-0.03}$	$-3.68^{+0.06}_{-0.07}$				
-21.25	$-3.39^{+0.03}_{-0.03}$	$-3.45^{+0.05}_{-0.06}$	$-3.64^{+0.02}_{-0.02}$	$-3.80^{+0.06}_{-0.06}$	$-3.72^{+0.06}_{-0.07}$			
-21.5	$-3.41^{+0.04}_{-0.04}$	$-3.60^{+0.03}_{-0.03}$	$-3.64^{+0.02}_{-0.02}$	$-3.80^{+0.03}_{-0.03}$	$-3.88^{+0.04}_{-0.04}$	$-3.83^{+0.06}_{-0.08}$		
-21.75	$-3.47^{+0.04}_{-0.04}$	$-3.67^{+0.03}_{-0.03}$	$-3.72^{+0.02}_{-0.02}$	$-3.82^{+0.03}_{-0.04}$	$-3.91^{+0.04}_{-0.04}$	$-4.05^{+0.03}_{-0.03}$	$-3.87^{+0.05}_{-0.06}$	$-3.97^{+0.08}_{-0.10}$
-22	$-3.51^{+0.03}_{-0.04}$	$-3.70^{+0.03}_{-0.03}$	$-3.77^{+0.03}_{-0.03}$	$-3.91^{+0.03}_{-0.03}$	$-3.94^{+0.02}_{-0.03}$	$-4.04^{+0.03}_{-0.03}$	$-3.98^{+0.04}_{-0.05}$	$-4.17^{+0.04}_{-0.04}$
-22.25	$-3.60^{+0.03}_{-0.04}$	$-3.74^{+0.02}_{-0.03}$	$-3.83^{+0.07}_{-0.08}$	$-4.02^{+0.03}_{-0.03}$	$-4.08^{+0.03}_{-0.03}$	$-4.12^{+0.02}_{-0.03}$	$-4.06^{+0.04}_{-0.04}$	$-4.20^{+0.03}_{-0.03}$
-22.5	$-3.75^{+0.06}_{-0.07}$	$-3.87^{+0.03}_{-0.04}$	$-4.01^{+0.03}_{-0.03}$	$-4.13^{+0.03}_{-0.03}$	$-4.26^{+0.03}_{-0.03}$	$-4.21^{+0.04}_{-0.05}$	$-4.23^{+0.03}_{-0.03}$	$-4.34^{+0.03}_{-0.03}$
-22.75	$-3.59^{+0.08}_{-0.09}$	$-4.04^{+0.05}_{-0.06}$	$-4.21^{+0.03}_{-0.04}$	$-4.36^{+0.03}_{-0.04}$	$-4.39^{+0.04}_{-0.05}$	$-4.44^{+0.04}_{-0.04}$	$-4.36^{+0.03}_{-0.03}$	$-4.41^{+0.03}_{-0.04}$
-23	$-3.37^{+1.04}_{-3.37}$	$-4.33^{+0.09}_{-0.11}$	$-4.62^{+0.06}_{-0.06}$	$-4.67^{+0.05}_{-0.06}$	$-4.64^{+0.05}_{-0.05}$	$-4.57^{+0.04}_{-0.04}$	$-4.61^{+0.05}_{-0.05}$	$-4.74^{+0.04}_{-0.04}$
-23.25			$-4.87^{+0.11}_{-0.15}$	$-5.12^{+0.08}_{-0.10}$	$-4.98^{+0.08}_{-0.08}$	$-4.86^{+0.05}_{-0.06}$	$-4.75^{+0.05}_{-0.05}$	$-4.94^{+0.05}_{-0.05}$
-23.5				$-5.25^{+0.17}_{-0.29}$	$-5.36^{+0.12}_{-0.17}$	$-5.17^{+0.07}_{-0.09}$	$-5.11^{+0.06}_{-0.07}$	$-5.08^{+0.06}_{-0.06}$
-23.75					$-5.57^{+0.18}_{-0.32}$	$-5.39^{+0.09}_{-0.11}$	$-5.35^{+0.09}_{-0.11}$	$-5.27^{+0.11}_{-0.16}$
-24							$-5.67^{+0.15}_{-0.24}$	$-6.04^{+0.16}_{-0.27}$
-24.25							$-5.39^{+0.18}_{-0.31}$	$-5.59^{+0.23}_{-0.54}$

Notes. (1) Values are base 10 logarithm. (2) Luminosities and redshifts correspond to bin centres.

Table D3. Numerical values (and uncertainties) for the LRR-corrected, NUV LFs of WiggleZ galaxies.

z: M_{NUV}	0.125	0.175	0.225	0.275	0.325	0.375	0.425	0.475
−15.5	$-1.56^{+0.17}_{-0.28}$							
−15.75	$-2.10^{+0.16}_{-0.25}$							
−16	$-2.27^{+0.12}_{-0.16}$							
−16.25	$-2.62^{+0.05}_{-0.06}$							
−16.5	$-2.73^{+0.05}_{-0.05}$	$-2.17^{+0.11}_{-0.14}$						
−16.75	$-2.57^{+0.05}_{-0.06}$	$-2.59^{+0.05}_{-0.06}$						
−17	$-2.50^{+0.06}_{-0.07}$	$-2.85^{+0.06}_{-0.07}$	$-2.37^{+0.30}_{-2.37}$					
−17.25	$-2.65^{+0.08}_{-0.10}$	$-2.67^{+0.17}_{-0.29}$	$-2.60^{+0.07}_{-0.08}$					
−17.5	$-2.83^{+0.13}_{-0.18}$	$-2.79^{+0.06}_{-0.06}$	$-2.82^{+0.05}_{-0.06}$	$-1.99^{+0.18}_{-0.32}$				
−17.75	$-2.58^{+0.13}_{-0.18}$	$-2.65^{+0.06}_{-0.08}$	$-2.78^{+0.04}_{-0.05}$	$-2.69^{+0.06}_{-0.07}$				
−18	$-2.64^{+0.14}_{-0.20}$	$-2.73^{+0.10}_{-0.12}$	$-2.74^{+0.06}_{-0.07}$	$-2.85^{+0.05}_{-0.05}$	$-1.84^{+0.14}_{-0.22}$			
−18.25	$-3.26^{+0.25}_{-0.66}$	$-3.03^{+0.15}_{-0.22}$	$-2.75^{+0.07}_{-0.09}$	$-2.79^{+0.05}_{-0.06}$	$-2.63^{+0.05}_{-0.06}$			
−18.5		$-2.80^{+0.13}_{-0.18}$	$-2.67^{+0.10}_{-0.13}$	$-2.69^{+0.06}_{-0.07}$	$-2.69^{+0.07}_{-0.09}$	$-2.45^{+0.06}_{-0.07}$		
−18.75		$-2.96^{+0.18}_{-0.33}$	$-2.70^{+0.14}_{-0.20}$	$-2.63^{+0.07}_{-0.09}$	$-2.73^{+0.05}_{-0.06}$	$-2.73^{+0.03}_{-0.03}$	$-2.28^{+0.06}_{-0.07}$	
−19			$-3.20^{+0.16}_{-0.26}$	$-2.79^{+0.14}_{-0.20}$	$-2.63^{+0.05}_{-0.06}$	$-2.67^{+0.03}_{-0.04}$	$-2.75^{+0.03}_{-0.03}$	$-2.29^{+0.05}_{-0.05}$
−19.25			$-2.93^{+0.18}_{-0.31}$	$-2.99^{+0.14}_{-0.21}$	$-2.65^{+0.07}_{-0.08}$	$-2.63^{+0.04}_{-0.04}$	$-2.80^{+0.03}_{-0.03}$	$-2.78^{+0.02}_{-0.02}$
−19.5			$-3.31^{+0.24}_{-0.58}$	$-3.43^{+0.24}_{-0.59}$	$-2.90^{+0.10}_{-0.13}$	$-2.62^{+0.05}_{-0.05}$	$-2.73^{+0.05}_{-0.06}$	$-2.84^{+0.02}_{-0.02}$
−19.75				$-2.81^{+0.20}_{-0.38}$	$-3.01^{+0.13}_{-0.18}$	$-2.83^{+0.07}_{-0.09}$	$-2.81^{+0.03}_{-0.04}$	$-2.88^{+0.02}_{-0.02}$
−20				$-2.89^{+1.04}_{-2.89}$	$-3.44^{+0.20}_{-0.38}$	$-3.04^{+0.09}_{-0.11}$	$-2.84^{+0.06}_{-0.07}$	$-2.93^{+0.03}_{-0.03}$
−20.25				$-3.14^{+1.04}_{-3.14}$	$-3.50^{+0.24}_{-0.55}$	$-3.14^{+0.12}_{-0.16}$	$-3.22^{+0.08}_{-0.10}$	$-3.12^{+0.04}_{-0.04}$
−20.5						$-3.39^{+0.16}_{-0.26}$	$-3.36^{+0.12}_{-0.17}$	$-3.38^{+0.07}_{-0.08}$
−20.75						$-2.83^{+0.27}_{-0.91}$	$-3.64^{+0.19}_{-0.34}$	$-3.57^{+0.09}_{-0.11}$
−21						$-3.52^{+1.04}_{-3.52}$	$-3.98^{+0.23}_{-0.54}$	$-3.85^{+0.14}_{-0.21}$
−21.25							$-3.67^{+0.23}_{-0.54}$	$-4.13^{+0.23}_{-0.54}$
−21.75							$-3.67^{+1.04}_{-3.67}$	

z: M_{NUV}	0.525	0.575	0.625	0.675	0.725	0.775	0.825	0.875
−19.25	$-2.26^{+0.07}_{-0.09}$							
−19.5	$-2.84^{+0.02}_{-0.02}$	$-2.41^{+0.09}_{-0.11}$						
−19.75	$-2.93^{+0.02}_{-0.02}$	$-3.05^{+0.02}_{-0.02}$	$-2.72^{+0.09}_{-0.12}$					
−20	$-2.98^{+0.02}_{-0.02}$	$-3.17^{+0.02}_{-0.02}$	$-3.17^{+0.02}_{-0.02}$	$-3.07^{+0.05}_{-0.06}$				
−20.25	$-3.06^{+0.02}_{-0.03}$	$-3.24^{+0.02}_{-0.02}$	$-3.35^{+0.02}_{-0.02}$	$-3.46^{+0.02}_{-0.02}$	$-3.35^{+0.03}_{-0.04}$	$-3.20^{+0.09}_{-0.11}$		
−20.5	$-3.28^{+0.03}_{-0.04}$	$-3.42^{+0.02}_{-0.02}$	$-3.51^{+0.02}_{-0.02}$	$-3.61^{+0.02}_{-0.02}$	$-3.66^{+0.02}_{-0.02}$	$-3.70^{+0.02}_{-0.02}$	$-3.52^{+0.04}_{-0.05}$	$-3.41^{+0.10}_{-0.12}$
−20.75	$-3.53^{+0.05}_{-0.06}$	$-3.70^{+0.03}_{-0.04}$	$-3.76^{+0.02}_{-0.03}$	$-3.79^{+0.03}_{-0.03}$	$-3.84^{+0.02}_{-0.02}$	$-3.90^{+0.02}_{-0.02}$	$-3.88^{+0.02}_{-0.03}$	$-3.88^{+0.03}_{-0.03}$
−21	$-3.94^{+0.09}_{-0.12}$	$-3.91^{+0.05}_{-0.05}$	$-4.10^{+0.03}_{-0.03}$	$-4.16^{+0.03}_{-0.03}$	$-4.05^{+0.03}_{-0.03}$	$-4.03^{+0.05}_{-0.05}$	$-4.00^{+0.03}_{-0.03}$	$-4.08^{+0.03}_{-0.03}$
−21.25	$-4.06^{+0.12}_{-0.16}$	$-4.11^{+0.07}_{-0.08}$	$-4.51^{+0.05}_{-0.05}$	$-4.50^{+0.04}_{-0.05}$	$-4.40^{+0.04}_{-0.04}$	$-4.28^{+0.03}_{-0.03}$	$-4.20^{+0.05}_{-0.05}$	$-4.26^{+0.03}_{-0.04}$
−21.5	$-4.17^{+0.17}_{-0.27}$	$-4.52^{+0.12}_{-0.17}$	$-4.74^{+0.07}_{-0.08}$	$-4.75^{+0.08}_{-0.09}$	$-4.66^{+0.07}_{-0.09}$	$-4.63^{+0.05}_{-0.05}$	$-4.50^{+0.06}_{-0.07}$	$-4.60^{+0.05}_{-0.05}$
−21.75	$-4.50^{+0.23}_{-0.54}$	$-4.68^{+0.16}_{-0.25}$	$-5.51^{+0.14}_{-0.21}$	$-5.16^{+0.13}_{-0.21}$	$-5.13^{+0.08}_{-0.10}$	$-4.99^{+0.08}_{-0.09}$	$-4.76^{+0.11}_{-0.15}$	$-4.66^{+0.15}_{-0.24}$
−22		$-4.88^{+0.20}_{-0.38}$	$-5.72^{+0.18}_{-0.30}$	$-5.67^{+0.16}_{-0.24}$	$-5.26^{+0.13}_{-0.19}$	$-5.13^{+0.09}_{-0.12}$	$-5.27^{+0.10}_{-0.13}$	$-5.13^{+0.09}_{-0.12}$
−22.25		$-5.13^{+1.04}_{-5.13}$	$-5.54^{+0.27}_{-0.82}$	$-5.89^{+0.18}_{-0.30}$	$-6.07^{+0.23}_{-0.55}$	$-5.72^{+0.18}_{-0.32}$	$-5.54^{+0.14}_{-0.20}$	$-5.36^{+0.13}_{-0.18}$
−22.5			$-6.32^{+1.04}_{-6.32}$	$-6.18^{+1.04}_{-6.18}$	$-5.75^{+0.19}_{-0.33}$	$-6.16^{+0.25}_{-0.62}$	$-6.09^{+0.29}_{-1.30}$	$-5.99^{+0.22}_{-0.45}$
−22.75			$-6.07^{+0.24}_{-0.59}$	$-6.51^{+1.04}_{-6.51}$	$-6.41^{+1.04}_{-6.41}$	$-5.87^{+0.26}_{-0.78}$	$-5.36^{+0.26}_{-0.74}$	$-6.52^{+1.04}_{-6.52}$
−23						$-6.20^{+1.04}_{-6.20}$	$-5.92^{+0.27}_{-0.89}$	$-6.16^{+1.04}_{-6.16}$
−23.25								$-6.50^{+1.04}_{-6.50}$

Notes. (1) Values are base 10 logarithm. (2) Luminosities and redshifts correspond to bin centres.

Table D4. Numerical values (and uncertainties) for the LRR-corrected, *r*-band LFs of WiggleZ galaxies.

z: M_r	0.125	0.175	0.225	0.275	0.325	0.375	0.425	0.475
−16	$-1.75^{+0.23}_{-0.54}$							
−16.25	$-3.25^{+0.24}_{-0.61}$							
−16.5	$-2.86^{+0.11}_{-0.14}$							
−16.75	$-2.95^{+0.08}_{-0.10}$							
−17	$-2.97^{+0.09}_{-0.11}$	$-2.92^{+0.25}_{-0.68}$						
−17.25	$-2.70^{+0.11}_{-0.14}$	$-3.15^{+0.11}_{-0.16}$						
−17.5	$-2.66^{+0.08}_{-0.11}$	$-3.09^{+0.07}_{-0.08}$						
−17.75	$-2.82^{+0.06}_{-0.07}$	$-3.06^{+0.10}_{-0.13}$	$-2.97^{+0.20}_{-0.37}$					
−18	$-2.51^{+0.08}_{-0.10}$	$-3.06^{+0.07}_{-0.09}$	$-3.24^{+0.07}_{-0.09}$					
−18.25	$-2.58^{+0.09}_{-0.11}$	$-3.07^{+0.07}_{-0.08}$	$-3.36^{+0.05}_{-0.06}$					
−18.5	$-2.45^{+0.09}_{-0.11}$	$-2.86^{+0.07}_{-0.09}$	$-3.17^{+0.05}_{-0.06}$	$-3.48^{+0.10}_{-0.13}$				
−18.75	$-2.48^{+0.12}_{-0.16}$	$-2.80^{+0.07}_{-0.08}$	$-3.10^{+0.04}_{-0.05}$	$-3.39^{+0.06}_{-0.07}$	$-2.37^{+0.23}_{-0.51}$			
−19	$-2.25^{+0.13}_{-0.19}$	$-2.85^{+0.07}_{-0.08}$	$-3.08^{+0.05}_{-0.08}$	$-3.32^{+0.05}_{-0.06}$	$-3.28^{+0.10}_{-0.12}$			
−19.25	$-2.28^{+0.22}_{-0.48}$	$-2.79^{+0.10}_{-0.13}$	$-2.89^{+0.07}_{-0.09}$	$-3.11^{+0.05}_{-0.05}$	$-3.24^{+0.18}_{-0.31}$	$-3.31^{+0.10}_{-0.12}$		
−19.5		$-2.59^{+0.17}_{-0.29}$	$-2.76^{+0.10}_{-0.13}$	$-2.99^{+0.06}_{-0.08}$	$-3.21^{+0.03}_{-0.04}$	$-3.38^{+0.06}_{-0.07}$	$-2.51^{+0.28}_{-1.00}$	
−19.75		$-2.52^{+0.12}_{-0.17}$	$-2.60^{+0.10}_{-0.14}$	$-2.93^{+0.06}_{-0.07}$	$-3.02^{+0.03}_{-0.15}$	$-3.24^{+0.03}_{-0.04}$	$-3.42^{+0.05}_{-0.06}$	
−20		$-2.12^{+0.15}_{-0.23}$	$-2.83^{+0.11}_{-0.14}$	$-2.92^{+0.08}_{-0.10}$	$-2.95^{+0.06}_{-0.07}$	$-3.11^{+0.03}_{-0.04}$	$-3.43^{+0.03}_{-0.04}$	$-3.29^{+0.06}_{-0.07}$
−20.25			$-2.70^{+0.09}_{-0.12}$	$-2.80^{+0.08}_{-0.10}$	$-2.94^{+0.06}_{-0.06}$	$-3.06^{+0.03}_{-0.03}$	$-3.21^{+0.03}_{-0.03}$	$-3.37^{+0.03}_{-0.04}$
−20.5			$-2.36^{+0.15}_{-0.23}$	$-2.57^{+0.15}_{-0.22}$	$-2.72^{+0.08}_{-0.10}$	$-3.03^{+0.04}_{-0.04}$	$-3.16^{+0.03}_{-0.03}$	$-3.28^{+0.03}_{-0.03}$
−20.75			$-1.79^{+0.24}_{-0.57}$	$-2.76^{+0.12}_{-0.16}$	$-2.71^{+0.06}_{-0.07}$	$-2.61^{+0.19}_{-0.36}$	$-3.02^{+0.04}_{-0.04}$	$-3.20^{+0.02}_{-0.02}$
−21				$-2.09^{+0.19}_{-0.34}$	$-2.78^{+0.07}_{-0.09}$	$-2.69^{+0.06}_{-0.07}$	$-2.95^{+0.04}_{-0.05}$	$-3.15^{+0.03}_{-0.03}$
−21.25				$-1.94^{+1.04}_{-1.94}$	$-2.52^{+0.06}_{-0.08}$	$-2.63^{+0.06}_{-0.08}$	$-2.79^{+0.04}_{-0.05}$	$-3.10^{+0.03}_{-0.03}$
−21.5					$-2.56^{+0.12}_{-0.17}$	$-2.55^{+0.07}_{-0.09}$	$-2.79^{+0.06}_{-0.07}$	$-2.95^{+0.03}_{-0.03}$
−21.75						$-2.62^{+0.07}_{-0.09}$	$-2.84^{+0.04}_{-0.04}$	$-2.89^{+0.03}_{-0.04}$
−22						$-2.38^{+0.14}_{-0.22}$	$-2.87^{+0.10}_{-0.14}$	$-3.03^{+0.04}_{-0.05}$
−22.25							$-2.57^{+0.12}_{-0.16}$	$-3.18^{+0.05}_{-0.05}$
−22.5								$-3.17^{+0.08}_{-0.09}$

z: M_r	0.525	0.575	0.625	0.675	0.725	0.775	0.825	0.875
−20.25	$-3.39^{+0.07}_{-0.08}$							
−20.5	$-3.51^{+0.03}_{-0.03}$	$-3.47^{+0.07}_{-0.09}$						
−20.75	$-3.33^{+0.04}_{-0.05}$	$-3.66^{+0.03}_{-0.04}$	$-3.46^{+0.06}_{-0.07}$					
−21	$-3.28^{+0.02}_{-0.02}$	$-3.57^{+0.02}_{-0.02}$	$-3.72^{+0.03}_{-0.03}$	$-3.68^{+0.06}_{-0.07}$				
−21.25	$-3.27^{+0.03}_{-0.03}$	$-3.43^{+0.06}_{-0.07}$	$-3.64^{+0.02}_{-0.02}$	$-3.80^{+0.06}_{-0.06}$	$-3.72^{+0.06}_{-0.07}$			
−21.5	$-3.11^{+0.04}_{-0.04}$	$-3.47^{+0.03}_{-0.03}$	$-3.64^{+0.02}_{-0.02}$	$-3.80^{+0.03}_{-0.03}$	$-3.88^{+0.04}_{-0.04}$	$-3.83^{+0.06}_{-0.08}$		
−21.75	$-3.04^{+0.03}_{-0.04}$	$-3.37^{+0.03}_{-0.03}$	$-3.61^{+0.02}_{-0.02}$	$-3.80^{+0.03}_{-0.04}$	$-3.91^{+0.04}_{-0.04}$	$-4.05^{+0.03}_{-0.03}$	$-3.87^{+0.05}_{-0.06}$	$-3.97^{+0.08}_{-0.10}$
−22	$-3.07^{+0.03}_{-0.03}$	$-3.33^{+0.03}_{-0.03}$	$-3.57^{+0.02}_{-0.03}$	$-3.80^{+0.03}_{-0.03}$	$-3.92^{+0.02}_{-0.03}$	$-4.04^{+0.03}_{-0.03}$	$-3.98^{+0.04}_{-0.05}$	$-4.17^{+0.04}_{-0.04}$
−22.25	$-3.14^{+0.03}_{-0.04}$	$-3.37^{+0.02}_{-0.03}$	$-3.56^{+0.08}_{-0.10}$	$-3.86^{+0.03}_{-0.03}$	$-3.99^{+0.03}_{-0.03}$	$-4.11^{+0.02}_{-0.02}$	$-4.06^{+0.04}_{-0.04}$	$-4.20^{+0.03}_{-0.03}$
−22.5	$-3.44^{+0.04}_{-0.05}$	$-3.50^{+0.03}_{-0.03}$	$-3.74^{+0.03}_{-0.03}$	$-3.92^{+0.03}_{-0.03}$	$-4.08^{+0.03}_{-0.03}$	$-4.14^{+0.05}_{-0.05}$	$-4.22^{+0.03}_{-0.03}$	$-4.33^{+0.03}_{-0.03}$
−22.75	$-3.35^{+0.08}_{-0.09}$	$-3.82^{+0.05}_{-0.05}$	$-3.95^{+0.03}_{-0.03}$	$-4.16^{+0.03}_{-0.03}$	$-4.18^{+0.04}_{-0.05}$	$-4.29^{+0.04}_{-0.04}$	$-4.30^{+0.03}_{-0.03}$	$-4.39^{+0.03}_{-0.04}$
−23	$-3.03^{+1.04}_{-3.03}$	$-4.12^{+0.09}_{-0.11}$	$-4.50^{+0.05}_{-0.05}$	$-4.45^{+0.05}_{-0.05}$	$-4.43^{+0.04}_{-0.04}$	$-4.37^{+0.03}_{-0.04}$	$-4.50^{+0.04}_{-0.04}$	$-4.62^{+0.04}_{-0.04}$
−23.25			$-4.61^{+0.13}_{-0.18}$	$-4.97^{+0.08}_{-0.09}$	$-4.72^{+0.06}_{-0.07}$	$-4.62^{+0.05}_{-0.05}$	$-4.55^{+0.05}_{-0.05}$	$-4.75^{+0.05}_{-0.05}$
−23.5				$-4.80^{+0.18}_{-0.30}$	$-5.06^{+0.10}_{-0.13}$	$-4.81^{+0.07}_{-0.09}$	$-4.75^{+0.07}_{-0.08}$	$-4.80^{+0.06}_{-0.07}$
−23.75					$-4.89^{+0.18}_{-0.33}$	$-4.94^{+0.09}_{-0.12}$	$-4.99^{+0.09}_{-0.11}$	$-4.75^{+0.08}_{-0.10}$
−24							$-4.96^{+0.16}_{-0.25}$	$-5.82^{+0.16}_{-0.26}$
−24.25							$-4.52^{+0.18}_{-0.31}$	$-4.87^{+0.28}_{-1.07}$

Notes. (1) Values are base 10 logarithm. (2) Luminosities and redshifts correspond to bin centres.

Table D5. The parameters describing the model that is the best analytic description of the WiggleZ NUV LFs. The parameters $\phi*$, $M*$ and α are the usual Schechter function parameters. The three power-law parameters describe the luminosity at which the LF transitions from a Schechter function to a power law. The QSO scaling parameter shows the contribution of quasars to each redshift's LF. When the best-fitting model does not include either a power-law transition or a quasar contribution, the parameters are flagged as N/A. The difference in χ^2 for the standard Schechter function, extended Schechter function, Schechter+quasar and extended+quasar models is presented in that order in the last column.

z	$\phi*$	$M*$	α	Power-law transition	Power-law slope	Power-law constant	Quasar scaling	Reduced χ^2	Models $\Delta\chi^2$
0.125	$-2.50^{0.07}_{-0.08}$	$-17.18^{0.25}_{-0.25}$	-1	N/A	N/A	N/A	N/A	1.2 (14.9/12)	0.0 2.0 2.0 4.0
0.175	$-2.60^{0.07}_{-0.08}$	$-17.45^{0.20}_{-0.20}$	-1	N/A	N/A	N/A	N/A	1.5 (14.8/10)	0.0 1.6 2.0 3.5
0.225	$-2.77^{0.05}_{-0.05}$	$-18.28^{0.17}_{-0.17}$	-1	N/A	N/A	N/A	N/A	0.7 (7.7/11)	0.0 1.9 2.0 3.9
0.275	$-2.65^{0.05}_{-0.06}$	$-18.17^{0.11}_{-0.11}$	-1	N/A	N/A	N/A	N/A	1.0 (12.1/12)	0.0 1.8 2.0 3.8
0.325	$-2.63^{0.05}_{-0.05}$	$-18.57^{0.10}_{-0.10}$	-1	N/A	N/A	N/A	N/A	0.6 (6.4/10)	0.0 2.0 2.0 4.0
0.375	$-2.67^{0.03}_{-0.03}$	$-19.12^{0.08}_{-0.08}$	-1	N/A	N/A	N/A	N/A	2.3 (25.7/11)	0.0 1.9 2.0 4.0
0.425	$-2.70^{0.03}_{-0.04}$	$-19.39^{0.09}_{-0.09}$	-1	N/A	N/A	N/A	N/A	2.2 (26.5/12)	0.0 1.8 2.0 3.8
0.475	$-2.63^{0.03}_{-0.04}$	$-19.42^{0.07}_{-0.07}$	-1	N/A	N/A	N/A	N/A	4.0 (39.6/10)	0.0 2.0 2.0 4.0
0.525	$-2.66^{0.04}_{-0.04}$	$-19.65^{0.08}_{-0.08}$	-1	N/A	N/A	N/A	N/A	3.4 (37.2/11)	0.0 0.2 2.0 2.3
0.575	$-2.71^{0.03}_{-0.03}$	$-19.58^{0.04}_{-0.04}$	-1	$-20.74^{0.12}_{-0.09}$	1.16	20.14	N/A	1.3 (15.3/12)	5.0 0.0 3.4 2.0
0.625	$-2.59^{0.03}_{-0.03}$	$-19.44^{0.04}_{-0.04}$	-1	N/A	N/A	N/A	$0.50^{0.17}_{-0.17}$	1.2 (15.1/13)	6.7 1.6 0.0 2.0
0.675	$-2.77^{0.03}_{-0.04}$	$-19.59^{0.03}_{-0.03}$	-1	$-21.09^{0.09}_{-0.07}$	1.59	28.94	N/A	1.5 (17.7/12)	6.5 0.0 1.7 2.0
0.725	$-2.82^{0.04}_{-0.05}$	$-19.68^{0.04}_{-0.04}$	-1	$-21.22^{0.09}_{-0.07}$	1.65	30.32	N/A	1.5 (16.0/11)	6.7 0.0 0.9 2.0
0.775	$-3.05^{0.04}_{-0.04}$	$-19.91^{0.05}_{-0.05}$	-1	$-21.43^{0.10}_{-0.07}$	1.62	29.86	N/A	1.1 (13.6/12)	5.6 0.0 1.0 2.0
0.825	$-3.07^{0.05}_{-0.06}$	$-20.02^{0.06}_{-0.06}$	-1	N/A	N/A	N/A	$0.17^{0.08}_{-0.08}$	1.4 (15.9/11)	3.0 1.2 0.0 2.0
0.875	$-3.12^{0.06}_{-0.07}$	$-20.03^{0.06}_{-0.06}$	-1	$-21.43^{0.09}_{-0.06}$	1.45	26.39	N/A	0.8 (9.3/12)	9.6 0.0 2.6 2.1

Table D6. The parameters describing the model that is the best analytic description of the WiggleZ *r* LFs. The parameters $\phi*$, $M*$ and α are the usual Schechter function parameters. The three power-law parameters describe the luminosity at which the LF transitions from a Schechter function to a power law. The QSO scaling parameter shows the contribution of quasars to each redshift's LF. When the best-fitting model does not include either a power-law transition or a quasar contribution, the parameters are flagged as N/A. The fitting results for $\alpha = -0.5$ are substituted when an $\alpha = -1$ fit could not be made. The difference in χ^2 for the standard Schechter function, extended Schechter function, Schechter+quasar and extended+quasar models is presented in that order in the last column.

z	$\phi*$	$M*$	α	Power-law transition	Power-law slope	Power-law constant	Quasar scaling	Reduced χ^2	Models $\Delta\chi^2$
0.125	$-2.42^{0.03}_{-0.04}$	$-18.64^{0.32}_{-0.32}$	-0.5	N/A	N/A	N/A	N/A	0.6 (8.9/14)	0.0 1.0 2.0 3.0
0.175	$-3.09^{0.06}_{-0.07}$	$-22.09^{4.82}_{-4.82}$	-1	N/A	N/A	N/A	N/A	0.5 (6.5/13)	0.0 1.8 2.0 3.8
0.225	$-3.13^{0.04}_{-0.04}$	$-20.24^{0.34}_{-0.34}$	-1	N/A	N/A	N/A	N/A	2.0 (26.1/13)	0.0 1.5 2.0 3.5
0.275	$-3.14^{0.04}_{-0.05}$	$-20.16^{0.22}_{-0.22}$	-1	N/A	N/A	N/A	N/A	4.8 (58.0/12)	0.0 1.5 2.0 3.5
0.325	$-2.98^{0.05}_{-0.05}$	$-20.20^{0.14}_{-0.14}$	-1	$-19.96^{0.18}_{-0.15}$	0.32	3.06	N/A	2.3 (27.6/12)	11.9 0.0 13.4 2.0
0.375	$-3.10^{0.03}_{-0.03}$	$-21.51^{0.24}_{-0.24}$	-1	$-20.56^{0.31}_{-0.28}$	0.17	0.10	N/A	4.4 (52.8/12)	2.6 0.0 4.6 2.0
0.425	$-3.24^{0.03}_{-0.03}$	$-22.07^{0.21}_{-0.21}$	-1	N/A	N/A	N/A	N/A	5.8 (69.6/12)	0.0 0.2 2.0 2.2
0.475	$-3.17^{0.02}_{-0.03}$	$-21.93^{0.13}_{-0.13}$	-1	$-21.20^{0.16}_{-0.15}$	0.21	0.92	N/A	3.8 (41.5/11)	8.2 0.0 10.0 2.0
0.525	$-3.29^{0.02}_{-0.02}$	$-22.68^{0.15}_{-0.15}$	-1	N/A	N/A	N/A	N/A	4.1 (49.1/12)	0.0 1.7 2.0 3.7
0.575	$-3.43^{0.02}_{-0.02}$	$-22.41^{0.08}_{-0.08}$	-1	N/A	N/A	N/A	N/A	2.9 (31.5/11)	0.0 5.5 2.0 7.5
0.625	$-3.38^{0.02}_{-0.02}$	$-21.92^{0.04}_{-0.04}$	-1	N/A	N/A	N/A	N/A	5.3 (58.5/11)	0.0 22.5 2.0 24.6
0.675	$-3.43^{0.02}_{-0.02}$	$-21.79^{0.04}_{-0.04}$	-1	N/A	N/A	N/A	N/A	1.8 (19.5/11)	0.0 42.8 2.0 44.9
0.725	$-3.51^{0.03}_{-0.03}$	$-21.87^{0.05}_{-0.05}$	-1	N/A	N/A	N/A	N/A	0.5 (6.0/11)	0.0 49.0 2.0 51.2
0.775	$-3.67^{0.02}_{-0.03}$	$-22.10^{0.04}_{-0.04}$	-1	N/A	N/A	N/A	N/A	1.0 (10.3/10)	0.0 102.2 2.0 104.6
0.825	$-3.59^{0.03}_{-0.04}$	$-22.05^{0.05}_{-0.05}$	-1	N/A	N/A	N/A	N/A	0.8 (8.3/11)	0.0 131.8 1.0 134.4
0.875	$-3.73^{0.03}_{-0.04}$	$-22.08^{0.05}_{-0.05}$	-1	N/A	N/A	N/A	N/A	1.6 (17.1/11)	0.0 185.8 1.6 188.9

Table D7. The parameters describing the model that is the best analytic description of the LRR-corrected, WiggleZ NUV LFs. The parameters $\phi*$, $M*$ and α are the usual Schechter function parameters. The three power-law parameters describe the luminosity at which the LF transitions from a Schechter function to a power law. The QSO scaling parameter shows the contribution of quasars to each redshift's LF. When the best-fitting model does not include either a power-law transition or a quasar contribution, the parameters are flagged as N/A. Fits for $\alpha = -0.5$ are substituted when a fit could not be achieved for $\alpha = -1$. The difference in χ^2 for the standard Schechter function, extended Schechter function, Schechter+quasar and extended+quasar models is presented in that order in the last column.

z	$\phi*$	$M*$	α	Power-law transition	Power-law slope	Power-law constant	Quasar scaling	Reduced χ^2	Models $\Delta\chi^2$
0.125	$-2.52^{0.05}_{-0.05}$	$-18.27^{0.45}_{-0.45}$	-1	N/A	N/A	N/A	N/A	2.0 (23.9/12)	0.0 2.0 2.0 4.0
0.175	$-2.34^{0.03}_{-0.03}$	$-17.94^{0.24}_{-0.24}$	-0.5	N/A	N/A	N/A	N/A	2.1 (20.9/10)	0.0 1.7 2.0 3.7
0.225	$-2.63^{0.05}_{-0.05}$	$-19.15^{0.37}_{-0.37}$	-1	N/A	N/A	N/A	N/A	0.9 (9.9/11)	0.0 2.0 2.0 4.0
0.275	$-2.63^{0.06}_{-0.06}$	$-19.41^{0.41}_{-0.41}$	-1	N/A	N/A	N/A	N/A	1.5 (18.0/12)	0.0 2.0 2.0 4.0
0.325	$-2.43^{0.05}_{-0.06}$	$-19.31^{0.19}_{-0.19}$	-1	N/A	N/A	N/A	N/A	1.3 (12.9/10)	0.0 2.0 2.0 4.0
0.375	$-2.52^{0.04}_{-0.04}$	$-20.09^{0.23}_{-0.23}$	-1	N/A	N/A	N/A	N/A	2.9 (31.5/11)	0.0 2.0 2.0 4.0
0.425	$-2.53^{0.04}_{-0.04}$	$-19.93^{0.15}_{-0.15}$	-1	N/A	N/A	N/A	N/A	3.2 (38.6/12)	0.0 1.9 2.0 3.9
0.475	$-2.48^{0.03}_{-0.03}$	$-19.75^{0.07}_{-0.07}$	-1	N/A	N/A	N/A	N/A	4.1 (40.6/10)	0.0 2.0 2.0 4.0
0.525	$-2.49^{0.02}_{-0.02}$	$-19.74^{0.05}_{-0.05}$	-1	N/A	N/A	N/A	N/A	3.2 (34.9/11)	0.0 0.4 1.9 2.4
0.575	$-2.62^{0.03}_{-0.03}$	$-19.72^{0.05}_{-0.05}$	-1	$-20.76^{0.13}_{-0.10}$	1.04	17.84	N/A	1.6 (19.6/12)	4.5 0.0 4.6 2.0
0.625	$-2.54^{0.02}_{-0.03}$	$-19.52^{0.03}_{-0.03}$	-1	N/A	N/A	N/A	$0.65^{0.25}_{-0.26}$	1.1 (13.9/13)	4.3 1.9 0.0 1.9
0.675	$-2.74^{0.03}_{-0.03}$	$-19.65^{0.03}_{-0.03}$	-1	$-21.05^{0.10}_{-0.07}$	1.46	26.35	N/A	1.7 (20.4/12)	7.1 0.0 2.2 2.0
0.725	$-2.85^{0.04}_{-0.05}$	$-19.78^{0.05}_{-0.05}$	-1	$-21.17^{0.11}_{-0.07}$	1.44	25.94	N/A	1.5 (16.5/11)	5.5 0.0 1.0 2.0
0.775	$-3.09^{0.04}_{-0.04}$	$-20.04^{0.05}_{-0.05}$	-1	$-21.38^{0.13}_{-0.09}$	1.38	24.85	N/A	1.1 (12.8/12)	3.9 0.0 1.3 2.0
0.825	$-3.21^{0.05}_{-0.05}$	$-20.24^{0.06}_{-0.06}$	-1	N/A	N/A	N/A	N/A	1.7 (18.8/11)	0.0 0.7 0.4 2.3
0.875	$-3.21^{0.06}_{-0.07}$	$-20.18^{0.07}_{-0.07}$	-1	$-21.41^{0.14}_{-0.09}$	1.24	22.01	N/A	0.8 (9.7/12)	4.0 0.0 2.2 2.0

Table D8. The parameters describing the model that is the best analytic description of the LRR-corrected, WiggleZ r LFs. The parameters $\phi*$, $M*$ and α are the usual Schechter function parameters. A Schechter function could only be fitted at all redshifts for $\alpha = -0.5$. No quasar contribution or shift to a power law was found, and the corresponding parameters are flagged N/A. The difference in χ^2 for the standard Schechter function, extended Schechter function, Schechter+quasar and extended+quasar models is presented in that order in the last column.

z	$\phi*$	$M*$	α	Power-law transition	Power-law slope	Power-law constant	Quasar scaling	Reduced χ^2	Models $\Delta\chi^2$
0.125	$-1.03^{1.90}_{-0.00}$	$-25.90^{170.67}_{-170.67}$	-0.5	N/A	N/A	N/A	N/A	0.9 (12.1/14)	0.0 2.0 2.0 4.0
0.175	$-1.31^{1.86}_{-0.00}$	$-26.29^{154.37}_{-154.37}$	-0.5	N/A	N/A	N/A	N/A	0.5 (6.7/13)	0.0 2.0 2.0 4.0
0.225	$-1.35^{1.93}_{-0.00}$	$-27.30^{181.02}_{-181.02}$	-0.5	N/A	N/A	N/A	N/A	1.6 (20.3/13)	0.0 2.0 2.0 4.0
0.275	$-1.40^{2.22}_{-0.00}$	$-27.91^{362.04}_{-362.04}$	-0.5	N/A	N/A	N/A	N/A	2.2 (25.8/12)	0.0 2.0 2.0 4.0
0.325	$-1.45^{1.63}_{-0.00}$	$-27.60^{90.51}_{-90.51}$	-0.5	N/A	N/A	N/A	N/A	2.1 (25.2/12)	0.0 1.9 2.0 3.9
0.375	$-1.51^{1.54}_{-0.00}$	$-27.79^{73.90}_{-73.90}$	-0.5	N/A	N/A	N/A	N/A	3.4 (41.3/12)	0.0 1.8 2.0 3.9
0.425	$-1.63^{1.34}_{-0.00}$	$-27.95^{45.25}_{-45.25}$	-0.5	N/A	N/A	N/A	N/A	6.0 (72.2/12)	0.0 1.8 2.0 3.8
0.475	$-2.65^{0.03}_{-0.03}$	$-22.99^{0.21}_{-0.21}$	-0.5	N/A	N/A	N/A	N/A	5.2 (57.2/11)	0.0 2.0 2.0 4.0
0.525	$-2.83^{0.01}_{-0.01}$	$-22.63^{0.12}_{-0.12}$	-0.5	N/A	N/A	N/A	N/A	9.7 (116.8/12)	0.0 2.0 2.0 4.1
0.575	$-3.09^{0.01}_{-0.01}$	$-22.18^{0.06}_{-0.06}$	-0.5	N/A	N/A	N/A	N/A	11.7 (128.2/11)	0.0 12.0 2.0 14.0
0.625	$-3.21^{0.01}_{-0.01}$	$-21.72^{0.03}_{-0.03}$	-0.5	N/A	N/A	N/A	N/A	11.5 (126.8/11)	0.0 36.4 2.0 38.4
0.675	$-3.31^{0.02}_{-0.02}$	$-21.65^{0.03}_{-0.03}$	-0.5	N/A	N/A	N/A	N/A	3.9 (42.7/11)	0.0 67.6 2.0 69.8
0.725	$-3.44^{0.02}_{-0.02}$	$-21.81^{0.04}_{-0.04}$	-0.5	N/A	N/A	N/A	N/A	0.5 (5.9/11)	0.0 60.2 2.0 62.3
0.775	$-3.63^{0.02}_{-0.02}$	$-22.10^{0.05}_{-0.05}$	-0.5	N/A	N/A	N/A	N/A	0.8 (8.3/10)	0.0 58.8 1.8 61.0
0.825	$-3.62^{0.03}_{-0.03}$	$-22.03^{0.06}_{-0.06}$	-0.5	N/A	N/A	N/A	N/A	2.7 (30.2/11)	0.0 26.3 1.1 28.5
0.875	$-3.70^{0.03}_{-0.03}$	$-21.93^{0.06}_{-0.06}$	-0.5	N/A	N/A	N/A	$0.56^{0.31}_{-0.31}$	3.0 (32.8/11)	1.3 134.8 0.0 137.3

This paper has been typeset from a TeX/LaTeX file prepared by the author.